NONLINEAR CONTROL OF MICROELECTROMECHANICAL SYSTEMS (MEMS) DEVICES.

by

KWADWO OSEI OWUSU

Presented to the Faculty of the Graduate School of

The University of Texas at Arlington in Partial Fulfillment

of the Requirements

for the Degree of

MASTER OF SCIENCE IN ELECTRICAL ENGINEERING

THE UNIVERSITY OF TEXAS AT ARLINGTON

August 2006

ACKNOWLEDGEMENTS

I am especially grateful to my advisor Dr. Frank L. Lewis for his enthusiasm, dynamism, guidance and support. I extend my appreciation to Dr. Jeongsik Sin for his tremendous help and ideas on pressure microsensors. I benefited enormously from his abundant knowledge of microsystems. Thanks are also due to Dr. Bruno Borovic and Dr. Ai Qun Liu, for useful discussions and encouragement. Further, I would like to thank Dr. Kai Yeung for being in my thesis committee. I thank all ARRI staff for providing a conducive and exciting learning environment. Finally, I wish to dedicate this work to my parents, for their lifelong support.

July 20, 2006

ABSTRACT

NONLINEAR CONTROL OF MICROELECTROMECHANICAL SYSTEMS (MEMS) DEVICES.

Publication No. _____

Kwadwo Owusu, M.S.

The University of Texas at Arlington, 2006

Supervising Professor: Dr. Frank L. Lewis

Different actuation principles have been developed for MEMS but electrostatic actuators are the most common. A significant drawback in the use of electrostatic actuators for some applications is their nonlinear voltage to position characteristics. Analog operation of these devices requires the use of feedback to stabilize and linearize them. Controlling and optimizing the operation of electrostatic controllers using feedback requires the establishment of the complete and accurate dynamical model of the device. In this thesis, we show how an optical switch driven by a MEMS electrostatic comb drive is controlled to guarantee its performance, stability and

reliability for use in optical networks. Analog control of electrostatically actuated MEMS devices is also discussed and analyzed. A simple 1-DOF actuator model is used to derive a nonlinear control scheme which eliminates “snap through” and improves the dynamic performance of electrostatic microactuators.

Finally, a novel fiber-optic pressure sensor design that employs a misaligned fiber-axis with respect to diaphragm center is discussed. It is shown that such a configuration increases the sensor sensitivity and pressure measurement range appreciably.

TABLE OF CONTENTS

LIST OF ILLUSTRATIONS

CHAPTER 1

INTRODUCTION

Microelectromechanical systems (MEMS) are the microscopic structures integrated onto silicon that combines mechanical elements, sensors and actuators with electronics. In a typical MEMS configuration, integrated circuits (ICs) provide the "thinking" part of the system, while MEMS complement this intelligence with active perception and control functions. MEMS are usually divided into two broad categories – sensor and actuators. Sensors gather local information from the environment including but not limited to mechanical, thermal, biological, chemical and optical phenomena. The electronics of the devices then process the information and direct actuators to respond and control the environment for some desired outcome.

The use of microfabrication techniques to create miniaturized sensors has become a subject of interest in many areas of science and engineering. The dominant micromachined sensors are pressure sensors. Compared to conventional macro scale sensors, micromachined sensors have improved performance, reduced size and reduced cost. Typically, the sensing element is a thin diaphragm which deflects with applied pressure. To measure the deflection, several sensing techniques including capacitance, piezoelectric and optical can be used. Using fiber-optic sensing has many inherent advantages including high sensitivity and immunity to electromagnetic interference

noise. Most fiber-optic sensors have fiber axis aligned with respect to the center of the diaphragm.

Numerous actuation methods have been developed for MEMS. They include magnetic, piezoelectric, thermal, optical and electrostatic actuators. Electrostatic actuators are the most common type of MEMS actuators because they are very low power, relatively simple in structure, flexible in operation and simple to fabricate. The fundamental principle behind electrostatic actuators is the coulomb force of attraction of two oppositely charged plates. Electrostatically actuated devices are used in such applications as optical switching, image projection, variable capacitors and accelerometers.

MEMS actuators are typically driven in an open loop fashion employing simple actuation signals. There are a number of techniques to improve the dynamic performance of MEMS devices under actuation. The simplest is to improve the mechanical design of the actuator to optimize its performance. Also, the dynamical model of the device can be used to construct pre-shaped actuation signals that have the potential to enhance the device performance appreciably. The lack of accurate dynamical models for pre-shaped input signal control and device fabrication limitations coupled with more stringent performance requirements have resulted tin the introduction of feedback control in MEMS. The first MEMS device employing feedback was closed-loop capacitive sensors, with the objective of enhancing measurement accuracy.

This thesis focuses primarily on MEMS actuators and sensors. Nonlinear control theory is used to design control systems for MEMS devices. Whereas linear control methods rely on the key assumption of small range operation for the linear model to be valid and are unsuitable for large range operation, nonlinear controllers can handle the nonlinearities in large range operation directly. Specifically, the reasons for using nonlinear control techniques are that the dynamics of the MEMS devices are inherently nonlinear, model uncertainties can be considered in the controller design and improved performance and robustness can be found. Controlling and optimizing the operation of MEMS devices with guaranteed performance, stability and reliability using nonlinear feedback control techniques requires the establishment of the complete and accurate dynamical model of the device.

Chapter 2 describes the design of a control scheme for an electrostatically actuated MEMS optical switch. The switch uses optical feedback for position sensing. The position cannot be easily obtained when the switch is near the fully opened or closed position due to the saturation in the available optical detector measurements. Also, the linear velocity of the switch required for feedback is very difficult and expensive to measure. A nonlinear full – order observer is therefore designed to provide reliable estimates of the position and velocity for feedback control. The designed controller is simulated on the actual device model and the results are presented.

In chapter 3, a nonlinear control method for analog control of electrostatic microactutators is presented. A simple 1-DOF model which completely captures the highly nonlinear voltage-to-position characteristics of electrostatic microactuators is

used in the analysis. This characteristic, often referred to as “pull-in” occurs due to destabilizing positive feedback in electrostatic actuation. The 1-DOF model is analyzed from a nonlinear controls perspective and an effective control law is established. The advantages of this controller include extending the range of motion, improved transient performance and improved analog control.

Chapter 4 describes the design of a novel fiber-optic pressure sensor that employs a misaligned fiber-axis with respect to diaphragm center. The primary objective is to try and eliminate multiple fringe ambiguity whilst extending the pressure measurement range and sensitivity of the device. It is shown that such a configuration increases the sensor sensitivity appreciably.

CHAPTER 2

NONLINEAR CONTROL OF A MEMS OPTICAL SWITCH

2.1 Introduction

The applications of Micro electro mechanical systems (MEMS) in optical networks have seen tremendous growth in recent years. This is partly due to the need for micro optomechanical switches (optical switches), a key component in optical communication networks.

Optical fibers in optical communication networks have very wide bandwidth. Large scale matrix switches that are mostly used in optical networks now are realized by optical – electronic conversion / electronic switching / electronic – optical conversion (O-E-O). These switches are very expensive and have slow bit rates capacity than fiber transmission lines due to the limited switching capacity of the electronics involved. With the increased demand for bandwidth due to the rapid growth of the information superhighway, it has become absolutely imperative to confront the bandwidth limitation problem. The obvious solution is to avoid the transitions between optical and electronic transmitters by using optical switches which operates in an all optical medium.

The optical switch is a device that switches an optical signal from one optical fiber to another, without having to first convert the optical signal into an electrical signal. This leads to the total exclusion of electronics and thus makes possible the

realization of all-optical networks (AON). The motivation of all-optical networks is evident from the bandwidth of an optical communication link.

MEMS technology has become a promising approach for optical switches. With this approach, micro mirrors are fabricated to perform the switching function in an all optical medium. MEMS optical switches are very attractive because of its small size and weight. In addition, they are inherently fast, have low power consumption [1] and have low insertion loss. The batch processing techniques applied to fabricate MEMS optical switches lead to high-volume, low cost production [2]. More importantly, MEMS technology allows large matrix switches to be monolithically integrated on a single chip [1].

With increasing complexity of modern optical networks, controlling and optimizing the operation of optical switches with guaranteed performance, stability and reliability becomes a challenging task. Controlling the device requires the establishment of its full models, including the optical, mechanical and electrical models. The optical models deal with the relationship between the mirror position and the attenuation, while the mechanical and electrical models link the driving voltage with the mirror position. Their combination predicts the optical performances of the switch under electrostatic actuation.

In the control of the optical switch, it is necessary to dynamically estimate the switch position and velocity. These states cannot be easily obtained when the switch is near the fully opened or closed position due to the saturation in the available optical detector measurements. To overcome this obstacle, a full-order nonlinear state observer

is constructed to provide a reliable estimate of the optical switch position and velocity based on the optical detector measurement of the output light intensity (power). The application of state observers in MEMS control is not new. In [4] a reduced-order observer is used to estimate the velocity for feedback control of electrostatically actuated MEMS to eliminate "snap-through". The observer design in this paper is effective for the saturated output system and utilizes the Lipschitz property of the nonlinearities in the state and output equations of the MEMS switch. Observer design for systems with Lipschitz nonlinearities have been dealt with in [5] and [6]. These designs assumed that the system output is linear. In this paper, we present a simple nonlinear observer for a system with a Lipschitz nonlinearity in the output characteristics.

The estimated state variables are then used to design a controller for the optical switch. The controller designed has two components. A nonlinear control design approach called feedback linearization [3] is applied to compensate the nonlinearity in the system dynamics and a linear tracking controller component which ensures that the switch position tracks a desired reference trajectory generated by a desired command generator.

This chapter will be organized as follows. Section 2.2 will present a mathematical model of the MEMS device and dynamics for the observer and controller design. Section 2.3 will present a nonlinear observer design based on the MEMS device model, and the analysis of convergence is carried out based on Lyapunov stability analysis. Section 2.4 will present an integrated control scheme combining the nonlinear

controller and the observer design presented in section 2.3. Simulation results will be discussed in section 2.5 and conclusions are presented in section 2.6.

2.2 MEMS Device Model and Dynamics

The SEM of the MEMS optical switch is shown in Figure 1 [9]. It consists of an electrostatic comb drive actuator, the suspension beam, a shuttle to which is attached a shutter (micromirror) and optical fiber grooves.

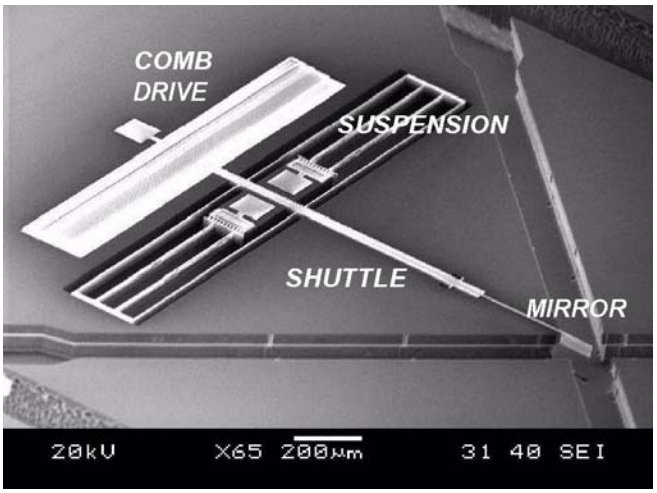

Figure 1.1 SEM of the MEMS Optical Switch showing its components.

The comb drive actuator consists of two sets of fingers with uniform gaps. One set of fingers is fixed and the other set of fingers is connected to the suspension and free to move relative to the fixed fingers. A voltage applied to the actuator generates an electrostatic force that moves the micromirror into the optical fiber beam path regulating the output power.

To model the system, it is assumed that the shuttle has only one degree of freedom. The mathematical model has three main components – mechanical, electrical

and optical models. The system can be described with a second order differential equation with input, output and system nonlinearities as

$$m\ddot{x} + d(\dot{x}, x) + k(x) = f(v, x); \quad P = h(x) \tag{2.1}$$

where m is the effective moving mass of the shuttle, d is the damping, k is the stiffness of the suspension, f is the induced electrostatic force, P is the light intensity and x the shuttle position.

2.2.1 Electrical Model

The electrical model considers the generation of the induced electrostatic force when a driving voltage is applied to the actuator. To find an expression for the force acting between the comb drive electrodes, the capacitance of the comb drive as a function of position is first determined. The capacitance of the comb drive is calculated as a sum of parallel capacitances among pairs of comb electrodes. Each pair of fingers forms a parallel capacitor. The total capacitance as a function of position x, is given by [7]

$$C(x) = \frac{\varepsilon_0 A}{d_G} = \frac{2n\varepsilon_0 T}{d_G}(x + x_0) \tag{2.2}$$

where $\varepsilon_0 = 8.854 \times 10^{-12} Fm^{-1}$ is the dielectric constant of vacuum, n is the number of movable comb fingers $(n = 150)$, T is the thickness of the structural layer $(T = 35\mu m)$, d_G is the length of the gap between fingers $(d_G = 2.6\mu m)$ and x_0 is the overlapped length of fingers at no applied voltage $(x_0 = 15\mu m)$. The capacitance of the comb drive at rest position is $C(0) = 0.5363\,pF$. The capacitance increases when the fingers are

attracted as a result of the electrostatic force induced on the application of a driving voltage. The electrostatic force between the electrodes of the capacitor is given as

$$f(v,x) = 0.5v^2 \frac{\partial C}{\partial x} \qquad (2.3)$$

where v is the applied voltage. Substituting (2) into (3), the electrostatic force can be expressed as

$$f(v,x) = \frac{n\varepsilon_0 T v^2}{d_G} = k_e v^2 \qquad (2.4)$$

where $k_e = 17.8nN/V^2$ is a constant.

The capacitance varies linearly with displacement, resulting in an electrostatic driving force which is independent of the position of the moving fingers (relative to the fixed ones) except at the ends of the range of travel.

2.2.2 Mechanical Model

To obtain the mechanical model of the system, the effective moving mass m, the damping coefficient d, and the stiffness of the suspension k are estimated. The effective mass of the movable structure can be expressed as [9]

$$m = m_{mirror} + 0.5m_{rigid} + 2.74m_{beam} \qquad (2.5)$$

From the geometry of the device and using the density of silicon $\rho_{Si} = 2.3\times10^3 kgm^{-3}$, the effective mass of the system is calculated as $m = 2.35\times10^{-9} kg$.

The stiffness of the suspension beam is assumed to be a linear function of the position i.e. $k(x) = kx$ and its coefficient is given as [9]

$$k = \frac{24EI_z}{L^3} = \frac{2ET(BW)^3}{(BL)^3} \tag{2.6}$$

where T is the thickness of the beam, E is the Young's modulus $(E = 160GPa)$, BW width of the suspension beams $(BW = 2\mu m)$, BL is length of suspension beams $(BL = 530\mu m)$ and I_Z moment of inertia around deflecting axis of the beam. Calculation gives $k = 0.6Nm^{-1}$.

Damping is the parameter that is most difficult to determine analytically, even through FEA. The reason lies in the number of different mechanisms that cause it, including friction, viscous forces, drag etc. The contribution of viscous forces to damping is much more pronounced. Four different mechanisms could contribute to damping, Couette flow, Poiseuille flow, Stokes flow, and squeeze film damping [11]. They can be summarized as $d(\dot{x}, x) = (d_x x + d_0)\dot{x}$. All four mechanisms contribute to d_0, but only Couette flow and squeeze film damping contribute to d_x. Poiseuille and Stokes flows are difficult to estimate due to the complex geometry of the device. Squeeze film damping is negligible. Hence, only Couette damping is considered. Couette damping is given as

$$d(\dot{x}, x) = \left(\frac{\eta A}{d_G}\right)\dot{x} = \left[\frac{\eta nT(x + x_0)}{d_G}\right]\dot{x} = (d_x x + d_x x_0)\dot{x} = (d_x x + d_0)\dot{x} \tag{2.7}$$

where $\eta = 18\mu Pa.s$ is the viscosity of the air surrounding the switch. The damping coefficients are calculated as $d_x = 0.0363$ and $d_0 = 5.4519 \times 10^{-7}$.

The complete analytical model is given by

$$2.35\times10^{-9}\,\ddot{x}+\left(0.0363x+5.4519\times10^{-7}\right)\dot{x}+0.6x=1.78\times10^{-8}\,v^2 \qquad (2.8)$$

2.2.3 Optical Model

The optical model relates the position of the mirror to the light intensity attenuation. Figure 2.2 shows the optical mirror and the input and output single mode fibers (SMF). Light beam from the input SMF propagates to the mirror plane and is partially blocked by the mirror. It is then diffracted to the receiving facet of the output SMF.

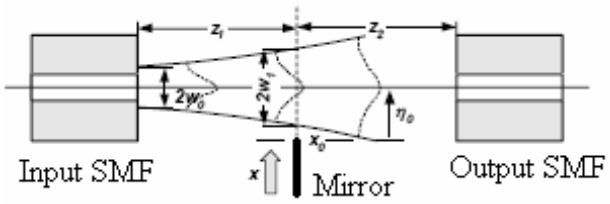

Figure 2.2 Diagram of Optical Model [8].

The model employed here is the Raleigh-Sommerfeld diffraction formula [10] which assumes a Gaussian distribution for the fundamental mode of the light beam from the SMFs. As illustrated in figure 2.2, the waist radius of the Gaussian beam coming from the input SMF is w_o. After passing through a distance z_1, the waist radius w_1 of the Gaussian beam is given by [8]

$$w_1 = w_o\sqrt{1+z_1^2/z_R^2} \qquad (2.9)$$

where z_R denotes the Raleigh range given by $z_R = \pi w_o^2 / \lambda$, λ represents the wavelength of light. In this example, $w_0 = 5.1\mu m$, $\lambda = 1.55\mu m$ and $z_1 = 10\mu m$. These parameters give $w_1 = 5.191\mu m$.

The coupled power P (P_{out} / P_{in}) is obtained [10] as

$$P = \frac{1}{2}\left[1 - Erf\left(\sqrt{2}(x - \eta_0) / w_1\right)\right] \qquad (2.10)$$

where η_0 is the initial distance between the mirror and the fiber axis, x is the displacement of the mirror and Erf is the error function. In this set up $\eta_0 = 11.2\mu m$. It is important to note that the shape of the attenuation curve (2.10) is saturated by the error function which makes it difficult to reconstruct the states in the saturation region for control design purposes.

2.2.4 Experimental Verification of the Model

The analytically obtained model is compared with experimental results obtained from the MEMS optical switch for accuracy.

The constant k_e in (2.4) can be verified by conducting static experiment i.e. $\ddot{x} = \dot{x} = 0$. Static conditions reduce (2.1) and (2.4) to $x = \frac{k_e}{k} v^2$. Different driving voltages are applied across the comb drive and its corresponding deflections observed through an optical microscope. Experimentally and analytically obtained static voltage-deflection curves are shown in Figure 2.3.

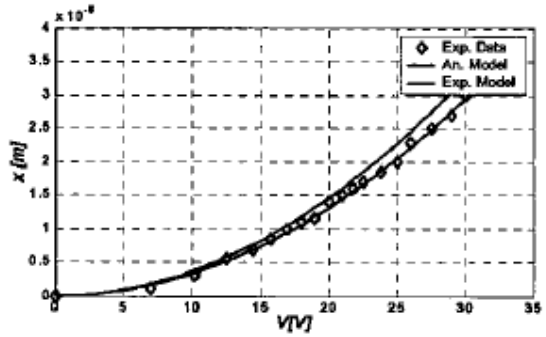

Figure 2.3 Static characteristics

The difference between the curves may be due to the estimation error of the gap between fingers d_G or the width of the suspension beam BW used in calculating the values of k_e and k respectively. The width of the suspension beam may be the likely culprit as it has a cubic effect on the stiffness, k.

To verify the optical model, a voltage is applied to the comb drive and light intensity is measured. Experimentally and analytically obtained coupled power-deflection curves are shown in figure 2.4. The difference in the two curves may be due to error in estimating η_0 in (2.10). This error can be modeled as an offset η_{off} which is determined to be about $2\mu m$.

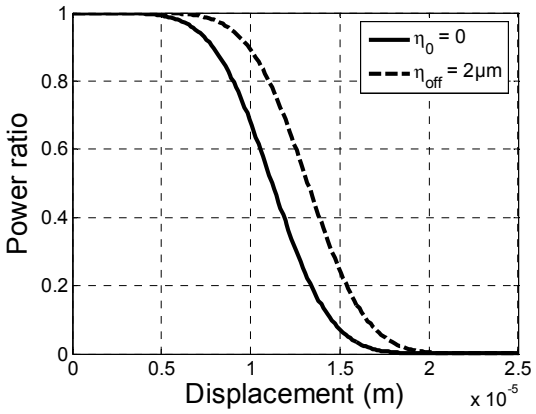

Figure 2.4 Verification of optical model.

For dynamic verification of the model, the open loop dynamic response of the switch is obtained by applying a square-wave driving voltage of 5-30V and measuring the light intensity. The obtained profile is compared with simulation results of the open loop dynamic response obtained from the developed model. The results are shown in figure 2.5.

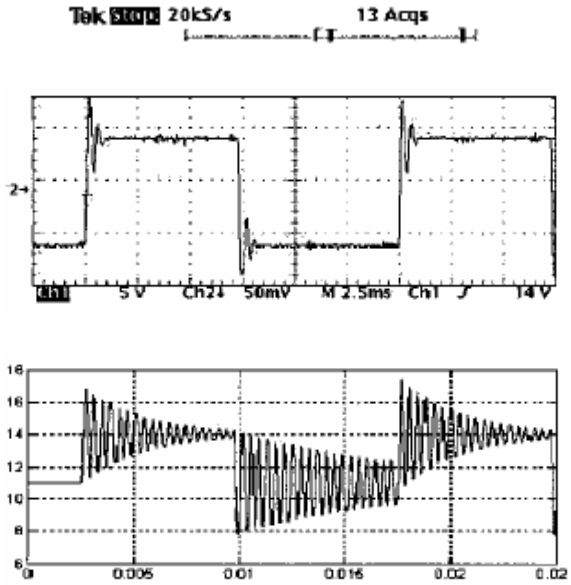

Figure 2.5 Experiment (top) and model (bottom) open loop dynamic response.

The results clearly show the underestimation of the damping component. This necessitates an identification of accurate model components.

2.2.5. Identification of Accurate Model Parameters

An identification of accurate parameters from the experimental results is carried out. The parameter identification procedure used in [12] is employed yielding the accurate dynamical model

$$2.35\times10^{-9}\ddot{x}+\left(0.0363x+1.6\times10^{-5}\right)\dot{x}+0.6x=1.8\times10^{-8}v^2 \qquad (2.11)$$

The parameters identified match closely with the analytical model except for the damping term which was underestimated.

2.3 Nonlinear Observer Design for the Saturated Output MEMS Optical Switch System

In this section, we will discuss a nonlinear observer design for the optical switch to estimate the switch position for feedback control. The problem is a saturated output, i.e. when the switch is completely closed or opened, due to the error function in the output measurement (2.10), position information required for feedback control cannot be obtained from the output measurement. The nonlinear observer presented here confronts this problem and serves to provide a reliable estimate of the switch position both inside and outside of the saturation region.

2.3.1. Observer Design

The dynamical model of the optical switch can be described by the nonlinear system

$$\dot{x} = Ax + Bu + \phi(x) \tag{2.12}$$

$$y = Cx + \theta(x) \tag{2.13}$$

where A, B, C are known linear parts about an equilibrium point, x_o and $\phi(x)$ and $\theta(x)$ are known locally Lipschitz nonlinearities at x_o i.e.,

$$\|\phi(x) - \phi(\hat{x})\| \le \gamma \|x - \hat{x}\| \tag{2.14}$$

$$\|\theta(x) - \theta(\hat{x})\| \le \beta \|x - \hat{x}\| \tag{2.15}$$

$\forall\, x, \hat{x} \in D(x_o, r) = \{x \in R^n \mid \|x - \hat{x}\| \le r\}$ with γ and β known Lipschitz constants.

$\theta(x)$ is obtained by linearizing the system output equation about x_o. The nonlinearity in the switch state dynamics can be regarded as Lipchitz, at least locally,

provided the operating range of x and $\dot{x}$ are guaranteed to be bounded. We assume that the pair (A,C) is observable. This is the case for the optical switch.

We create an observer with linear output injection of the form

$$\dot{\hat{x}} = A\hat{x} + Bu + \phi(\hat{x}) + L[C\hat{x} + \theta(\hat{x}) - Cx - \theta(x)] \tag{2.16}$$

The estimation error dynamics are then seen to be given by

$$\dot{\tilde{x}} = (A + LC)\tilde{x} + \phi(x) - \phi(\hat{x}) + L[\theta(x) - \theta(\hat{x})] \tag{2.17}$$

where $\tilde{x} = x - \hat{x}$. Equation (2.17) is linear with nonlinear perturbations and does not depend on the control input $u(t)$.

2.3.2. Stability Analysis

The stability of the proposed observer (2.16) is here analyzed. Since the pair (A,C) is completely observable, we can find a matrix L such that all eigenvalues of the matrix $(A + LC)$ are in the desired locations in the open left half plane. If we choose $(A + LC)$ to be Hurwitz, then for any positive definite Q_o, there exists a unique symmetric positive definite P_o which satisfies the Lyapunov equation

$$(A + LC)^T P_o + P_o (A + LC) = -2Q_o \tag{2.18}$$

Consider the Lyapunov function candidate

$$V_{obs}(\tilde{x}) = \tilde{x}^T P_o \tilde{x} \tag{2.19}$$

Its derivative along the trajectories of (2.17) is

$$\dot{V}_{obs} = \tilde{x}^T \left[(A + LC)^T P_o + P_o (A + LC)\right]\tilde{x} + 2\tilde{x}^T P_o [\phi(x) - \phi(\hat{x})] + 2\tilde{x}^T P_o L[\theta(x) - \theta(\hat{x})] \tag{2.20}$$

Using the Lipschitz property of $\phi(x)$ and $\theta(x)$, we have

$$2\tilde{x}^T P_o[\phi(x)-\phi(\hat{x})] \le 2\gamma\|P_o\|_2\|x\|_2^2 \tag{2.21}$$

$$2\tilde{x}^T P_o L[\theta(x)-\theta(\hat{x})] \le 2\beta\|L\|_2\|P_o\|_2\|\tilde{x}\|_2^2 \tag{2.22}$$

Substituting into (2.20), we get

$$\dot{V}_{obs} \le -2\tilde{x}^T Q_o\tilde{x} + 2\gamma\|P_o\|_2\|x\|_2^2 + 2\beta\|L\|_2\|P_o\|_2\|x\|_2^2 \tag{2.23}$$

Since Q_o is positive definite, $\tilde{x}^T Q_o\tilde{x} \ge \lambda_{\min}(Q_o)\|\tilde{x}\|_2^2$ where $\lambda_{\min}(Q_o)$ is the smallest eigenvalue of Q_o. Also, since P_o is symmetric positive definite, $\|P_o\|_2 = \lambda_{\max}(P_o)$ where $\lambda_{\max}(P_o)$ is the maximum eigenvalue of P_o. Substituting these into (2.23) yields

$$\dot{V}_{obs} \le -\left[2\lambda_{\min}(Q_o) - 2(\gamma+\beta\|L\|_2)\lambda_{\max}(P_o)\right]\|x\|_2^2 \tag{2.24}$$

Hence $\dot{V}_{obs} < 0$ if

$$\frac{\lambda_{\min}(Q_o)}{\lambda_{\max}(P_o)} > (\gamma+\beta\|L\|_2) \tag{2.25}$$

The ratio in (2.25) is a maximum when Q_o is the identity matrix [7]. Set $Q_o = I_2$, then a sufficient condition for $\dot{V}_{obs}$ to be negative is

$$\|L\|_2 < \frac{1}{\beta}\left[\frac{1}{\lambda_{\max}(P)} - \gamma\right] \tag{2.26}$$

If (2.26) is satisfied, then $\tilde{x} = 0$ is an asymptotically stable equilibrium point of (2.17) and the observer accurately reconstructs the state estimates.

2.3.3 Observer for MEMS Optical Switch

For the MEMS optical switch system $A=\begin{bmatrix} 0 & 1 \\ -k/m & -d_o/m \end{bmatrix}$, $B=\begin{bmatrix} 0 \\ k_e/m \end{bmatrix}$, $\phi(x)=\begin{bmatrix} 0 \\ -d_x x_1 x_2/m \end{bmatrix}$. An equilibrium point for the system is $x_1 = \frac{k_e U_0}{0.6}, x_2 = 0$ where $U_0 = v^2$ is the equilibrium control input. Selecting a suitable point $x_1 = 11.2\times10^{-6}$ in the linear region of the output light intensity curve, we compute the equilibrium control input as $U_0 = 373.33$. Linearizing the output characteristics about the equilibrium point, we obtain $C = [-0.24593 \quad 0]$. We then design the observer gain matrix such that the eigenvalues of $(A-LC)$ are appropriately placed and (2.26) is satisfied.

2.4 Nonlinear Observer-Controller Design

This section shows how we can replace the state x with the estimated state $\hat{x}$ from the observer in a nonlinear full state feedback linearization controller and still guarantee the stability of the closed loop observer-controller system.

2.4.1 Feedback Linearization Controller

Feedback linearization control is proposed to control the switch position. An estimate of the switch states from the observer is needed for feedback linearization compensation. With the nonlinear observer design discussed in section 2.3, an integrated control scheme is presented to combine the nonlinear controller and the observer. Figure 2.6 shows the block diagram of the integration of the nonlinear controller and the observer. A smooth desired trajectory $x_d = [x_d, \dot{x}_d, \ddot{x}_d]^T$ is generated from a proper reference trajectory generator. The objective of the controller is to

provide proper control action that enables the switch position to track the desired trajectory.

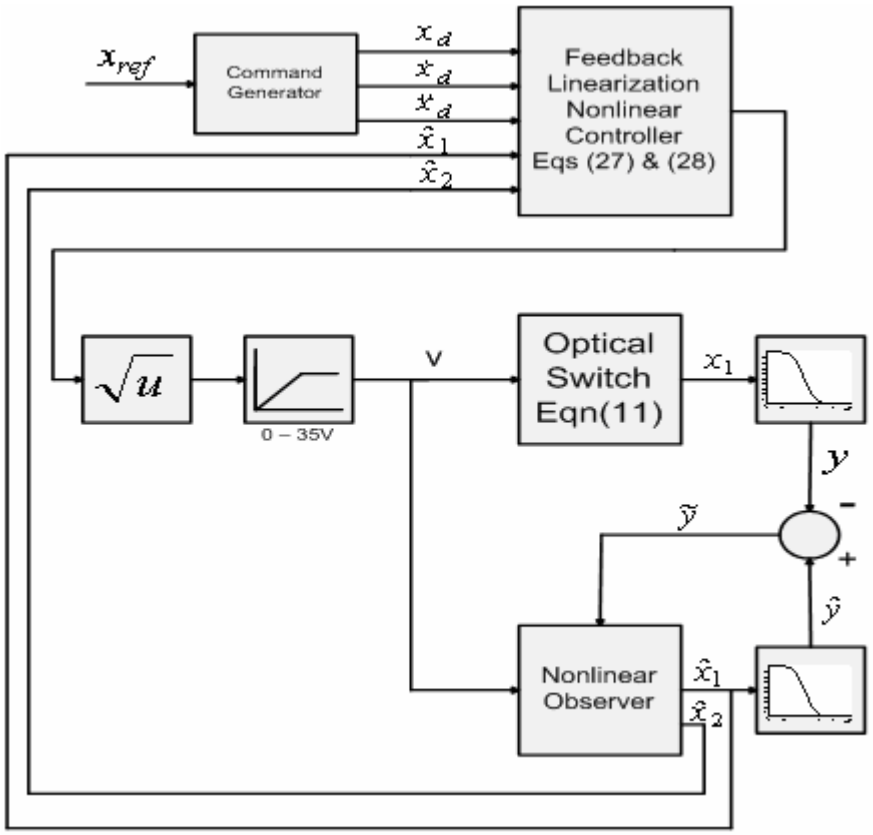

Figure 2.6 Block Diagram of the integration of the Controller and Observer.

The dynamics of the optical switch are

$$\dot{x}_1 = x_2$$
$$\dot{x}_2 = \frac{1}{m}\{[-kx_1 - (d_x x_1 + d_o)x_2] + k_e v^2\} \qquad (2.27)$$

where the voltage term v^2 is the control input.

The dynamics in (2.27) can be put in the form $\dot{x} = f(x) + g(x)u$. According to [8], any nonlinear system whose state space has dimension $n = 2$ can be transformed

into a linear system, via state feedback and change of coordinates, around a point x_o, if and only if the matrix $\begin{pmatrix} g(x_o) & ad_f g(x_o) \end{pmatrix}$ has rank 2. This condition is satisfied for the switch dynamics in (2.27).

We choose a nonlinear feedback control law of the form

$$v^2 = \frac{m}{k_e}\left[w - \frac{1}{m}\left[-k\hat{x}_1 - (d_x \hat{x}_1 + d_o)\hat{x}_2 \right] \right] \tag{2.28}$$

where the term w guarantees the tracking of the desired trajectory and $\hat{x}_1$, $\hat{x}_2$ are state estimates from the nonlinear observer. Since it is desired to have the switch position x_1, track a prescribed trajectory x_d, the term w in the control law can be specified as

$$w = \ddot{x}_d - a_1 \dot{\hat{e}}_1 - a_o \hat{e}_1 \tag{2.29}$$

where $\hat{e}_1 = \hat{x}_1 - x_d$.

We define the tracking error as $e_1 = x_1 - x_d$ and $e_2 = x_2 - \dot{x}_d$. The tracking error dynamics is given by

$$\begin{aligned} \dot{e}_1 &= e_2 \\ \dot{e}_2 &= -a_o e_1 - a_1 e_2 + (a_o - \frac{k}{m})\tilde{x}_1 + (a_1 - \frac{d_o}{m})\tilde{x}_2 \\ &\quad -\frac{d_x}{m}(x_1 x_2 - \hat{x}_1 \hat{x}_2) \end{aligned} \tag{2.30}$$

The tracking error dynamics can be written as

$$\dot{e} = A_c e + b\tilde{x} + \left[\phi(x) - \phi(\hat{x}) \right] \tag{2.31}$$

where

$$A_c = \begin{bmatrix} 0 & 1 \\ -a_o & -a_1 \end{bmatrix} \text{ and } b = \begin{bmatrix} 0 & 0 \\ a_o - k/m & a_1 - d_o/m \end{bmatrix}$$

2.4.2 Stability Analysis

Here, the stability analysis based on the closed loop system is performed. It is important to realize that the tracking error dynamics is driven by the observer estimation error terms which are exponentially decaying. It is also clear that as long as A_c is asymptotically stable, the tracking error will be bounded as long as the estimation errors are. The magnitude of the tracking error depends on the degree of stability of A_c as well as the magnitude of the estimation errors. A more stable A_c and proper observer convergence results in a smaller error.

To show the stability of the feedback linearization controller with estimated states, consider the Lyapunov function candidate for the controller

$$V_{con}(e) = e^T P_c e \tag{2.32}$$

Select A_c to be Hurwitz, then for any positive definite Q_c there exists a unique symmetric positive definite P_c which satisfies the Lyapunov equation

$$A_c{}^T P_c + P_c A = -2Q_c \tag{2.33}$$

The derivative of V_{con} along the trajectories of (30) is given by

$$\dot{V}_{con} = -e^T Q_c e + 2e^T P_c b\tilde{x} + 2e^T P_c[\phi(x) - \phi(\hat{x})] \tag{2.34}$$

Hence,

$$\dot{V}_{con} \le -\lambda_{\min}(Q_c)\|e\|_2^2 + 2\|e\|_2\|\tilde{x}\|_2\lambda_{\max}(P_c)\left(\|b\|_2 + \gamma\right) \tag{2.35}$$

where $\lambda_{\min}(Q_c)$ and $\lambda_{\max}(P_c)$ are minimum and maximum eigenvalues of Q_c and P_c respectively.

Now consider the composite Lyapunov function

$$V(\tilde{x}, e) = V_{con}(e) + V_{obs}(\tilde{x}) \tag{2.36}$$

for the total system (observer and controller). Then

$$\begin{aligned}\dot{V}(\tilde{x}, e) \le & -\lambda_{\min}(Q_c)\|e\|_2^2 + 2\|e\|_2\|\tilde{x}\|_2\lambda_{\max}(P_c)\left(\|b\|_2 + \gamma\right) \\ & -\left[\lambda_{\min}(Q_o) - 2\left(\gamma + \beta\|L\|_2\right)\lambda_{\max}(P_1)\right]\|\tilde{x}\|_2^2\end{aligned} \tag{2.37}$$

Manipulation of (2.37) results in

$$\dot{V}(\tilde{x}, e) \le -\begin{bmatrix}\|\tilde{x}\|_2 & \|e\|_2\end{bmatrix}[M]\begin{bmatrix}\|\tilde{x}\|_2 \\ \|e\|_2\end{bmatrix} \tag{2.38}$$

where

$$M = \begin{bmatrix}\lambda_{\min}(Q_o) - & -\lambda_{\max}(P_c)\left[\|b\|_2 + \gamma\right] \\ 2\left(\gamma + \beta\|L\|_2\right)\lambda_{\max}(P_o) & \\ -\lambda_{\max}(P_c)\left[\|b\|_2 + \gamma\right] & \lambda_{\min}(Q_c)\end{bmatrix} \tag{2.39}$$

For $\dot{V}(\tilde{x}, e)$ to be negative, it is sufficient that the leading principal minors of the $2x2$ matrix M be positive, that is

$$\lambda_{\min}(Q_o) - 2\left(\gamma + \beta\|L\|_2\right)\lambda_{\max}(P_o) > 0 \tag{2.40}$$

and

$$\lambda_{\min}(Q_c)\left[\lambda_{\min}(Q_o)-2\left(\gamma+\beta\|L\|_2\right)\lambda_{\max}(P_o)\right]\lambda^2{}_{\max}(P_c)\left(\|b\|_2+\gamma\right)^2>0 \tag{2.41}$$

Selecting $Q_o = Q_c = I_2$, in order for equations (2.40) and (2.41) to be satisfied, it is enough that

$$\|L\|_2 < \frac{1}{\beta}\left[\frac{1}{\lambda_{\max}(P)}-\gamma\right] \tag{2.42}$$

and

$$\|b\|_2 < \frac{\left[1-2\left(\gamma+\beta\|L\|_2\right)\lambda_{\max}(P_o)\right]^{1/2}}{\lambda_{\max}(P_c)}-\gamma \tag{2.43}$$

A nonlinear separation principle is not valid in this case as the controller parameters specified by $\|b\|_2$ are selected based on the observer gain.

2.5 Simulation Results

The performance of the proposed control scheme is simulated on the MEMS optical switch. The numerical simulation reported here is performed over a time interval of 2ms, with a variable integration step.

The reference signal used in the simulation is the output of the second order transfer function $\frac{1}{(\tau s+1)^2}$ driven by a pulse wave input. The choice of the time constant τ which determines the speed of motion from the initial to the final position is limited by the constraint on the magnitude of the control input $(V_{\max} = 35V)$.

The true initial state is $x_0 = [0\ 0]^T$ while the observed initial state is $x_0 = [1\mu m\ 0]^T$. Zero initial velocity is assumed for both observer and MEMS device to

mimic the practical situation of the MEMS device and the estimation process switching on at the same time.

The observer gain matrix used in the simulation is $L=\left[1.6255\times10^{6}\ 2.019\times10^{11}\right]^{T}$ and the tracking error components of the controller used were $a_0=1\times10^{12}$ and $a_1=2\times10^{6}$.

The time response of the system for a desired trajectory of amplitude 10μm and 25μm are shown in figures 2.7 and 2.8 respectively.

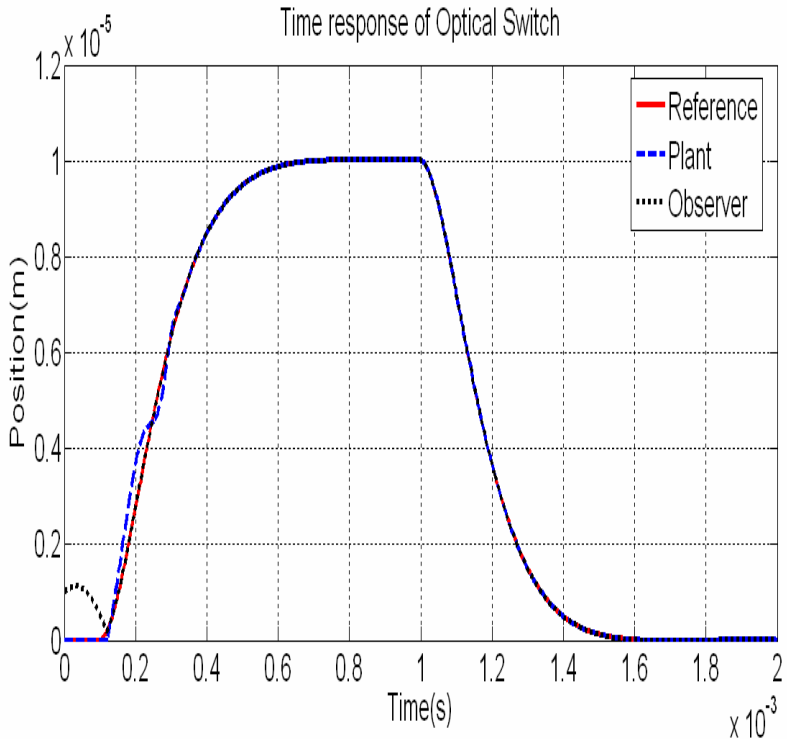

Figure 2.7 Response of the system to a desired reference signal of amplitude 10μm.

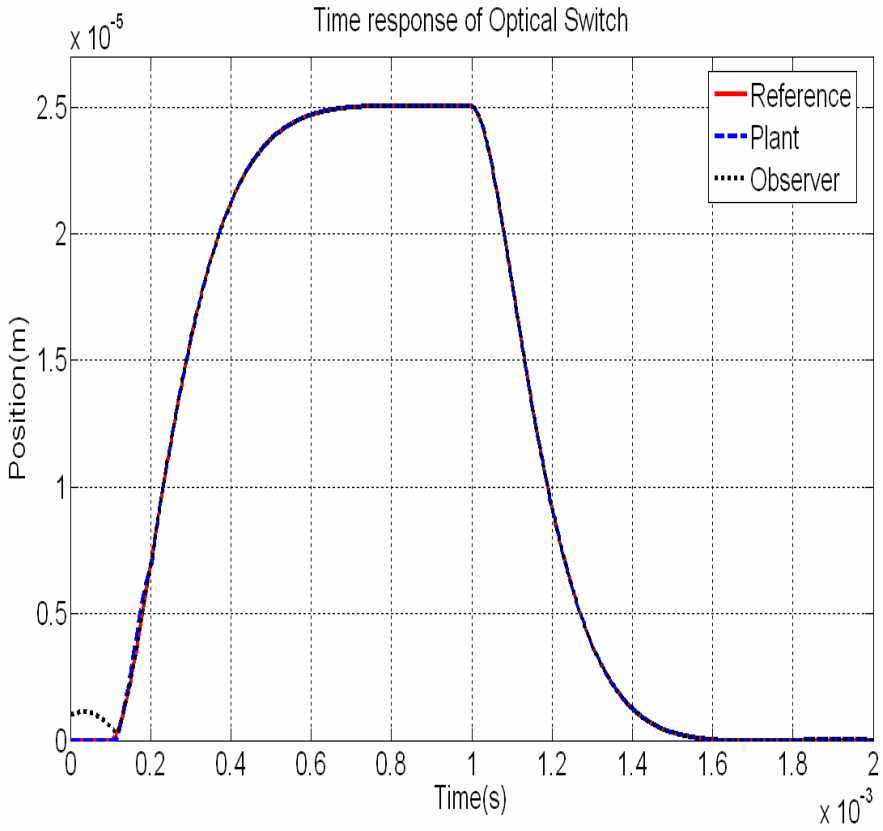

Figure 2.8 Response of the system to a desired reference signal of amplitude 25μm

The response shows a very fast response time with the rise time and falling time less than 0.6ms. The overshoot is almost negligible. It is observed that although the observer starts with different initial conditions its states converge to the actual states very quickly and the tracking of the reference signal is almost perfect. Also, the system performance is worse for small reference signals.

Now, we assume that the estimation of the model parameters used in the feedback linearization term and observer model have 20% error, specifically the

parameters m, d_x, d_0, k, k_e were reduced by 20%. Figures 2.10 and 2.11 show the time response for a desired trajectory of amplitude 10μm and 25μm respectively.

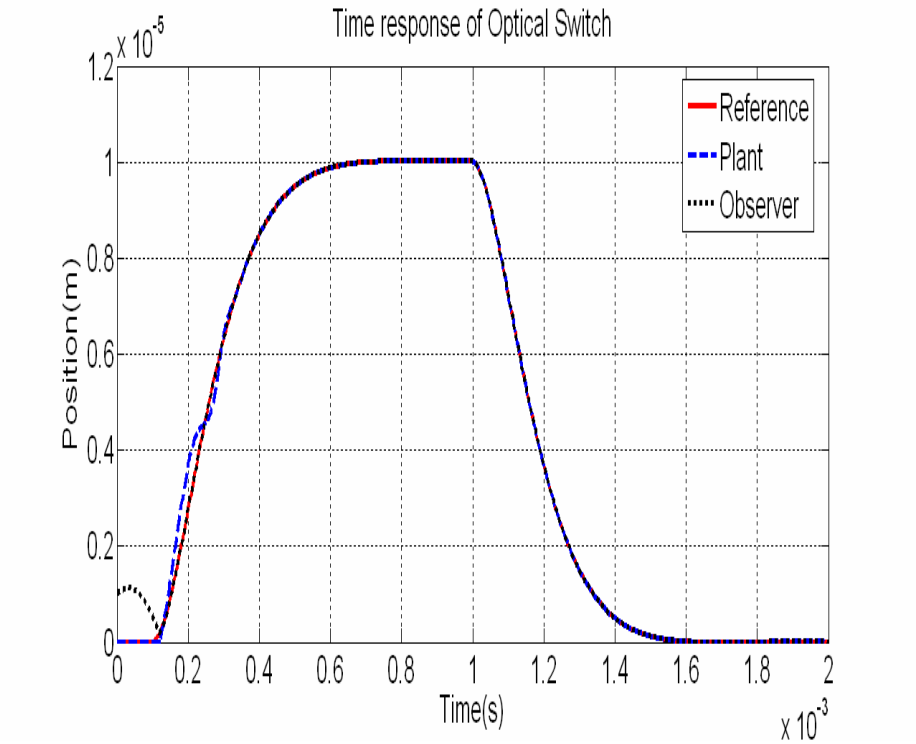

Figure 2.9 Observer model and feedback linearization has 20% error

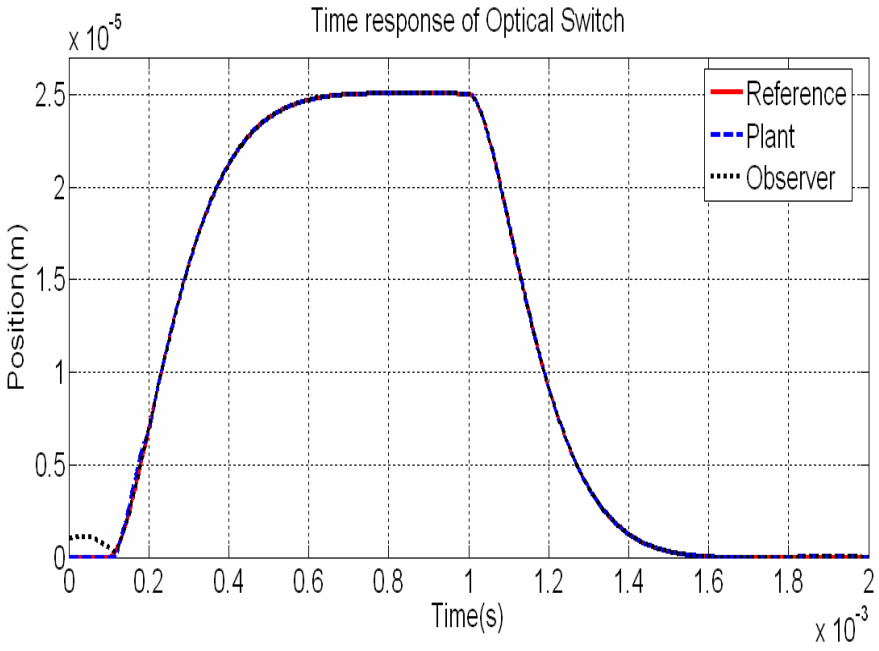

Figure 2.10 Observer model and feedback linearization has 20% error

A similar performance of the nonlinear observer-controller design is observed even for very large modeling uncertainties. This clearly demonstrates the robustness of this proposed design scheme.

2.6 Conclusions

A MEMS optical switch has been developed. Its dynamical model has been established based on the electrical, mechanical and optical models of the device. The model is verified by experimental results.

A nonlinear observer was designed to estimate the dynamic variables of the optical switch. Feedback linearization controller with estimated states from a nonlinear observer has been introduced to improve the dynamic closed loop performance of the

optical switch. The simulation demonstrates that even with large estimation error of the observer model and feedback linearization term, the nonlinear controller can still achieve the desired performance.

CHAPTER 3

NONLINEAR CONTROL OF ELECTROSTATIC MICROACTUATORS

3.1 Introduction

Parallel-plate electrostatically actuated devices play a vital role in MEMS. Compared with other types of microactuators, electrostatic actuators are the most common in use apparently because of the fact that they generate modest force and consume relatively no electrical power. Electrostatic actuators are normally driven by static open-loop voltage control schemes. A serious drawback in this control strategy is that a voltage source provides positive feedback in the electrostatic actuation. An increase in the constant voltage source results in a corresponding increase in electrostatic force due to an increase in the charge. The increased force decreases the gap, which, in turn, increases the capacitance and thus the charge and the electric field due to the applied voltage. This positive feedback causes the actuator to deflect further. At a distance of two-thirds of the zero-bias capacitive gap, the actuator position becomes unstable and collapses. This phenomenon is known as "snap-through" or "pull-in" [13], [14].

Thus, open-loop constant voltage drive is unable to provide stable and controllable deflection beyond 33% of the zero bias capacitive gap. This prohibits the suitability of this control scheme for devices that require an analog control of stable positions within the entire gap such as variable capacitors, wavelength division

multiplexing (WDM) filters and tunable LEDs [15]. For such applications, it is desirable to extend the stable and controllable stable range to the full gap.

It has been demonstrated that by placing a series capacitance in the DC path of the MEMS bridge circuit, the instability in the electrostatic actuation can be reduced and even eliminated [13]. A serious drawback with this actuation approach is the need for higher supply voltage required to reach any equilibrium position. Also, the performance of this control scheme is seriously affected by the natural damping of the device. Other suggested methods are based on structural design modifications such as, extending the capacitive gap to be much larger than the desired operating range [4], leverage and nonlinear stiffening springs [16], [17]. The tradeoff in employing these mechanical modifications is the need for higher voltages and a more tedious and complex fabrication process.

The significant limitations of the aforementioned control schemes have resulted in the gradual incorporation of closed-loop feedback control system driving techniques in extending the desired operation range of electrostatic microactuators. In [18] it is shown that any position in the gap may be globally asymptotically stabilized with output feedback of voltage and charge. A current drive control stabilization strategy that uses charge feedback to extend the range of electrostatic microactuators beyond the voltage pull-in point is proposed in [19].

The primary objective of this chapter is to demonstrate the feasibility of a robust nonlinear control scheme for electrostatic miroactuators using feedback. Stability and convergence analysis of the proposed controller is presented analytically. Simulation

results on the performance of the proposed feedback nonlinear controller on a MEMS electrostatic microactuator are presented.

This chapter will be organized as follows. Section 3.2 will present a mathematical model of the MEMS device and dynamics and discuss "pull-in" instability under electrostatic actuation. Section 3.3 will present a nonlinear controller design with model based feedback linearization and the analysis of convergence is carried out based on Lyapunov stability analysis. Section 3.4 will present a nonlinear reduced order velocity observer design required to implement the controller in section 3.3. Section 3.5 will analyze the stability of the integrated control scheme combining the nonlinear controller and observer design. Simulation results will be discussed in section 3.6 and conclusions are presented in section 3.7.

3.2 MEMS Device Model and "Pull-in" Instability Analysis

3.2.1 Device Model

The microactuator is modeled as a parallel plate capacitor consisting of a movable top plate and a fixed plate as shown in figure 3.1. The mechanical part of the microactuator is modeled as a spring-mass-damper system.

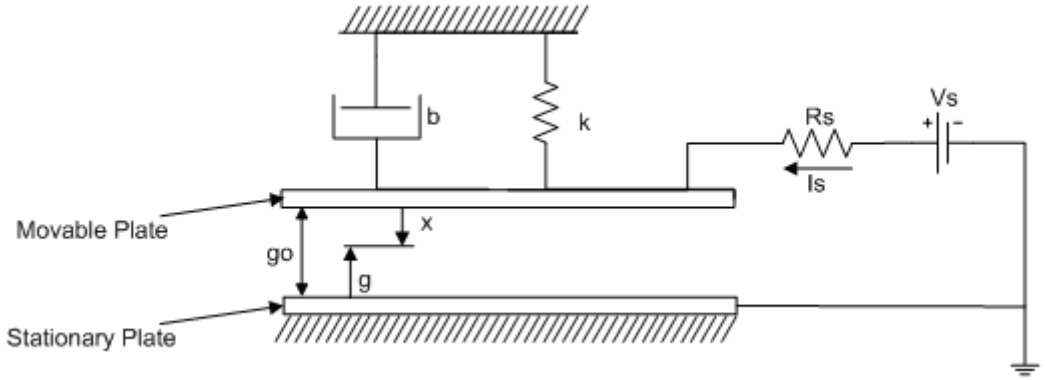

Figure 3.1 1 - Dimensional Model of MEMS Electrostatic Microactuator

When a voltage is applied between the plates, an electrostatic force is induced on the movable plate. The governing equation for the 1-D model is

$$m\ddot{x}+b\dot{x}+kx=F_e \qquad (3.1)$$

where F_e is the electrostatic pull-down force exerted on the movable plate by the applied voltage V_s, k is the mechanical stiffness, b is the damping factor and m the equivalent mass of the movable plate. The deflection of the movable plate is given by $x=g_0-g(t)$ where g_0 is the zero-bias capacitive gap and $g(t)$ it the applied voltage bias capacitive gap. Considering the electrostatic force in terms of the applied electric field, $F_e=QE/2$ where Q is the charge and $E=V/G$ is the electric field due to the applied voltage. The capacitance of the device is given by $C=\varepsilon A/g$ where ε is the permittivity in the gap and A is the plate area. Incorporating the expressions for $x, F_e, E \text{ and } C$ in (3.1), the complete equation of motion is given by (3.2)

$$m\ddot{g}(t)+b\dot{g}(t)+k(g(t)-g_0)=-Q^2(t)/2\varepsilon A \qquad (3.2)$$

Applying Kirchoff's Voltage law, the current through the input resistance is

$$\dot{Q}(t)=\frac{1}{R_s}\left[V_s(t)-\frac{Q(t)g(t)}{\varepsilon A}\right] \tag{3.3}$$

The complete model given by (3.2) and (3.3) is of third order.

3.2.2 "Pull-in" Instability Analysis

At equilibrium, the distance $x(t)$ traveled by the movable plate for any applied constant voltage is determined by the elastic stiffness and the magnitude of the applied voltage. From (3.2), the equilibrium relationship is

$$k(g(t)-g_0)=F_e \tag{3.4}$$

The electrostatic force applied to the movable plate is found by considering the power delivered to a time-dependent capacitance and is given by [20]

$$F_e=\frac{1}{2}V_s^2\frac{dC}{dg}=-\frac{1}{2}\frac{\varepsilon A V_s^2}{g^2} \tag{3.5}$$

From (3.4) and (3.5), the applied voltage at equilibrium is

$$V_s=\sqrt{\frac{2k}{\varepsilon A}g^2(g_0-g)} \tag{3.6}$$

Figure 3.2 shows a plot of applied voltage versus normalized plate deflection at equilibrium for a microactuator with plate area, $A=4\times10^{-8}m^2$, $g_0=6\times10^{-6}m$, and $k=10Nm^{-1}$.

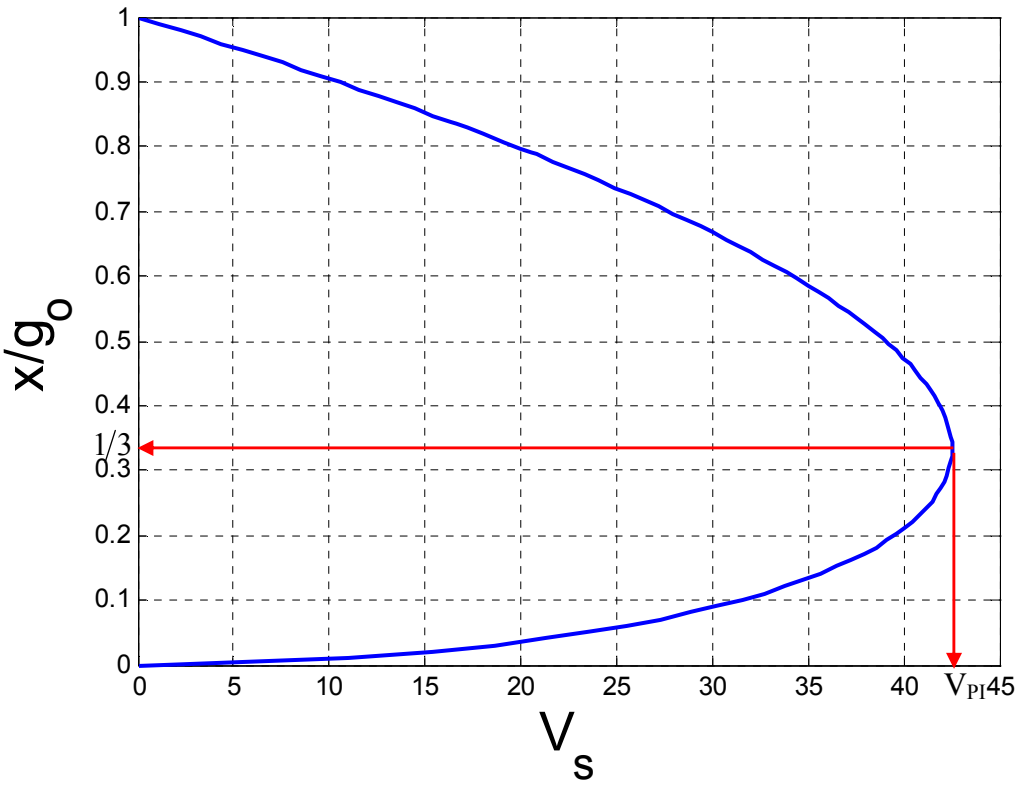

Figure 3.2 Normalized Plate Deflection vs. Applied Voltage

The plot shows that the system has two equilibrium points for applied voltages less than the "pull-in" voltage V_{PI} and zero beyond. At $x=\frac{1}{3}g_0$, the increase in the electrostatic force is greater than the increase in the restoring force resulting in the collapse of the movable plate to the fixed plate position. Taking the derivative of (3.6) with respect to g and setting to zero, the plate deflection at which "pull-in" instability occurs is found to be exactly one-third of the zero-bias capacitive gap and the "pull-in" voltage is found to be

$$V_{PI} = \sqrt{\frac{8k}{27\varepsilon A} g_0^3} \tag{3.7}$$

The point $x = \frac{1}{3} g_0$ at which "pull-in" instability occurs corresponds to a saddle-node bifurcation phenomenon with respect to the equilibrium voltage [4]. Thus, under equilibrium conditions with constant voltage operation, the movable plate can only move $1/3$ of the entire capacitive gap. Violating this restriction results in the plates snapping together which is undesirable for some applications.

One approach to overcome this travel range limitation whilst improving the dynamic performance of the MEMS device is to employ closed-loop feedback control voltage actuation techniques. For control design purposes, we perform a normalization of variables as follows [15].

$$X = x/g_0, \quad t = w_0 T, \quad q = Q/Q_{PI,} \quad u = V_S/V_{PI} \quad and \quad R = C_0 R_S \tag{3.8}$$

where $C_0 = \varepsilon A/g_0$ is the capacitance at rest, T is the time and

$$Q_{PI} = \frac{3C_0 V_{PI}}{2}, \quad V_{PI} = \sqrt{\frac{8kg_0^2}{27C_0}}, \quad w_0 = \sqrt{\frac{k}{m}}, \quad \alpha = \frac{b}{2mw_0} \tag{3.9}$$

Using the above normalization, equations (3.2) and (3.3) can be transformed into the normalized differential equations governing the moving plate dynamics as

$$\ddot{X} + 2\alpha\dot{X} + X = q^2/3 \tag{3.10}$$

$$\dot{q} = \frac{2}{3R}\left[u - \frac{3}{2}q(1 - X)\right] \tag{3.11}$$

Imposing the state transformation, $x_1 = X$, $x_2 = \dot{X}$ *and* $x_3 = q$, the system (3.10), (3.11) can be put in the state space form

$$\begin{bmatrix} \dot{x}_1 \\ \dot{x}_2 \\ \dot{x}_3 \end{bmatrix} = \begin{bmatrix} x_2 \\ -2\alpha x_2 - x_1 + x_3^2/3 \\ -x_3(1-x_1)/R \end{bmatrix} + \begin{bmatrix} 0 \\ 0 \\ 2/(3R) \end{bmatrix} u \qquad (3.12)$$

Since it is possible and relatively inexpensive to accurately measure the voltage and capacitance across the device, we consider as the system output, the normalized voltage, v_D and normalized charge, q (deduced from voltage and capacitance measurements) across the actuator. The system output is thus defined as

$$y_1 = 3x_3(1-x_1)/2 \qquad (3.13)$$

$$y_2 = x_3 \qquad (3.14)$$

Under equilibrium conditions, let the state x be denoted by x^*. For a given constant applied voltage, the equilibrium points are seen from (3.12), (3.13) and (3.14) to be given by $x^* = [x_1^*, 0, x_3^*]^T$ and $v_D^* = 3x_3^*(1-x_1^*)/2$. Also, for a given x_1^*, x_3^* is given by $x_3^* = \pm(3x_1^*)^{1/2}$. Therefore, for a given constant applied voltage, the system has three equilibrium points. The equilibrium point containing $x_3^* = -(3x_1^*)^{1/2}$ lies below the fixed plate which is outside the operation region of the device and is not considered. The other two equilibrium points lie inside the operation region. As shown in section 3.2.2 equilibrium points corresponding to an upper plate deflection less than one-third of the zero-voltage gap are stable, while those corresponding to an upper plate deflection greater than one-third of the zero-voltage gap are unstable points.

3.3 Nonlinear Controller Design with Model Based Feedback Linearization

The considered control problem is set-point control from any point in the gap to any other point between the plates. For a greater degree of freedom in designing a suitable controller, the system is considered as a SISO system with the output redefined as

$$y = x_1 = 1 - \frac{2y_1}{3y_2} \tag{3.15}$$

We consider the set point tracking problem with $y = x_1$ as output. To generate a linear input-output relation, we differentiate the output function y repeatedly until the input u appears and then design u to cancel the nonlinearities in the system [3]. From the system dynamics, define

$$f(x) = \begin{bmatrix} x_2 \\ -2\alpha x_2 - x_1 + x_3^2/3 \\ -x_3(1-x_1)/R \end{bmatrix}, \quad g(x) = \begin{bmatrix} 0 \\ 0 \\ 2/(3R) \end{bmatrix}, \quad \text{and} \quad h(x) = x_1$$

Denoting the Lie derivative by L we have,

$$L_g h(x) = 0, \quad L_g L_f h(x) = 0, \quad L_g L_f^2 h(x) = \frac{4}{9R} x_3$$

$$L_f h(x) = x_2, \quad L_f^2 h(x) = -2\alpha x_2 - x_1 + \frac{1}{3} x_3^2$$

$$L_f^3 h(x) = 2\alpha x_1 + (4\alpha^2 - 1)x_2 - \frac{2}{3}\left(\alpha + \frac{1}{R}\right)x_3^2 + \frac{2}{3R} x_1 x_3^2$$

From the Lie derivatives, for the input u to appear, the output function $y = x_1$ has to be differentiated three times to obtain

$$y^{(3)} = L_f^3\, h(x) + L_g L_f^2 h(x) u \qquad (3.16)$$

Thus, with respect to this output, the system has a well-defined relative degree of 3 (equal to the system order) at each point such that $x_3 \neq 0$. Around any of such points, there is no internal dynamics associated with the input-output linearization and the system can be transformed into a linear and controllable system by means of the feedback control law [3].

$$u = \frac{1}{L_g L_f^2 h(x)} \left(- L_f^3\, h(x) + v \right) \qquad (3.17)$$

Substituting (3.17) into (3.16) yields the simple linear relation

$$y^{(3)} = v \qquad (3.18)$$

To design the tracking controller, we assume that a desired trajectory $y_r = \left[y_r, \dot{y}_r, \ddot{y}_r, y_r^{(3)} \right]$ is generated from a proper reference trajectory generator. A linear control law is constructed for the system (3.19) as

$$v = y_r^{(3)} - k_3 \ddot{e} - k_2 \dot{e} - k_1 e \qquad (3.19)$$

where $e = y - y_r$ is the tracking error. The tracking error dynamics is seen to be given by

$$e^{(3)} + k_3 \ddot{e} + k_2 \dot{e} + k_1 e = 0 \qquad (3.20)$$

The error function $e(t)$ satisfies a linear differential equation of order 3, whose coefficients can be arbitrarily preset. The coefficients $k_i \, (i = 1, 2, 3)$ are chosen such that the characteristic equation associated with (3.20)

$$A(s) = s^3 + k_3 s^2 + k_2 s + k_1 \qquad (3.21)$$

has all its roots strictly in the left hand plane. Using the Routh-Hurwitz stability criterion, the coefficients should be selected as $k_1 > 0, k_3 > 0, k_2 > k_1/k_3$. Therefore, under the effect of an input of the form (3.17), the output of the system tracks the desired output $y_r(t)$ with an error which can be made to converge to zero, as $t \to \infty$, with arbitrarily fast exponential decay.

The physical control input u is given by

$$u = \frac{9R}{4x_3}\left[-2\alpha x_1 - \left(4\alpha^2 - 1\right)x_2 - \frac{2}{3R}x_1 x_3^2 + \frac{2}{3}\left(\alpha + \frac{1}{R}\right)x_3^2 + y_r^{(3)} - k_3\ddot{e} - k_2\dot{e} - k_1 e \right] \tag{3.22}$$

The feedback control input u is undefined at $x_3 = 0$. $x_3 = 0$ means there is no charge across the device and hence the induced electrostatic force and applied voltage are zero. Under these conditions, the system is at rest with $x_1 = x_2 = x_3 = 0$. The system (3.12) is inherently stable at the origin under zero voltage bias. Therefore, the control (3.22) will stabilize the system in all gaps except at the origin, where it is adequate to remove the control input.

The implementation of this feedback control law requires the measurement of the device velocity x_2 . The measurement of the velocity is very costly and difficult. A reduced order nonlinear state observer is thus constructed to provide a reliable estimate of the velocity for feedback.

3.4 Nonlinear Reduced-Order State Observer Design for Velocity

The voltage and capacitance across the device can be easily and accurately measured at a relatively low cost. From these measurements, the charge across the device (x_3) and the deflection of the movable plate (x_1) are easily deductible. However, the measurement of the device velocity is relatively costly and difficult. A reduced order state observer that reliably and accurately estimates the device velocity with arbitrarily fast error dynamics is constructed to confront this problem.

A possible reduced order observer for x_2 is constructed by prior coordinate transformation similar to that used in linear reduced order observer design [21]. We define a state observer utilizing the nonlinear model for the device velocity with a linear injection term as

$$\dot{\bar{x}}_2 = -2\alpha\,\hat{x}_2 - x_1 + x_3^2/3 - k_d\hat{x}_2 \tag{3.23}$$

$$\hat{x}_2 = \bar{x}_2 + k_d x_1 \tag{3.24}$$

where $\hat{x}_2$ is the observer estimate.

3.4.1 Observer Estimation Error Dynamics

Differentiating (3.24) results in the observer dynamics

$$\dot{\hat{x}}_2 = -2\alpha\hat{x}_2 - x_1 + x_3^2/3 + k_d\left(x_2 - \hat{x}_2\right) \tag{3.25}$$

Even though the dynamics of $\dot{\hat{x}}_2$ contains x_2 (the unknown state variable), the actual computation of the observer is done using (3.23) and (3.24) and hence x_2 is not explicitly used. The observer estimation error dynamics is given by

$$\dot{\tilde{x}}_2 = -(2\alpha + k_d)\tilde{x}_2 \qquad (3.26)$$

where $\tilde{x}_2 = x_2 - \hat{x}_2$ is the estimation error.

3.4.2 Stability Analysis

The stability of the proposed observer (3.23), (3.24) is here analyzed using Lyapunov theory. Consider the Lyapunov function candidate

$$V_{obs}(\tilde{x}_2) = \frac{1}{2}\tilde{x}_2^2 \qquad (3.27)$$

Its derivative along the trajectories of (3.26) is

$$\dot{V}_{obs}(\tilde{x}_2) = \tilde{x}_2\dot{\tilde{x}}_2 = -(2\alpha + k_d)\tilde{x}_2^2 \qquad (3.28)$$

Utilizing the useful property $x_2^2(t) \le \|\tilde{x}_2(t)\|^2$ and letting $\beta = (2\alpha + k_d)$ we obtain

$$\dot{V}_{obs}(\tilde{x}_2) \le -\beta\|\tilde{x}_2(t)\|^2 \qquad (3.29)$$

where $\|.\|$ denotes the L^2 - norm. If $\beta > 0$, we see that $\dot{V}_{obs}(\tilde{x}_2) < 0$, $\forall \tilde{x}_2 \neq 0$ and the equilibrium point $\tilde{x}_2 = x_2 - \hat{x}_2 = 0$ is uniform globally exponentially stable.

3.5 Cascaded Nonlinear Observer-Controller Design

In this section, we show how we can replace the state x_2 with the estimated state $\hat{x}_2$ from the observer in the nonlinear full state feedback linearization based controller and still guarantee the stability of the closed-loop observer-controller system.

The tracking error dynamics (3.20) can be put in the equivalent state space form $\dot{e} = Ae$ where $A = \begin{bmatrix} 0 & 1 & 0 \\ 0 & 0 & 1 \\ -k_1 & -k_2 & -k_3 \end{bmatrix}$. If we replace the state x_2 with the estimated state

$\hat{x}_2$ from the nonlinear reduced order observer in the feedback control law (3.22), the perturbed system is given by

$$\dot{e} = Ae + b\tilde{x}_2 \tag{3.30}$$

where $b = \begin{bmatrix} 0 & 0 & k_3(2\alpha + k_d) - 4\alpha^2 + 1 - k_2 \end{bmatrix}^T$.

It is important to realize that the tracking error dynamics is driven by the observer estimation error term which is exponentially decaying. It is also clear that as long as A is asymptotically stable, the tracking error will be bounded as long as the estimation error is. The magnitude of the tracking error depends on the degree of stability of A as well as the magnitude of the estimation error. A more stable A and proper observer convergence results in a smaller tracking error. From a practical point of view, we impose a stringent, critical condition limiting the growth rate of $\tilde{x}_2$. It is assumed that the perturbation term $b\tilde{x}_2$ satisfies the relation

$$\|bx_2\| \le \delta \|\tilde{x}_2\| \quad \forall \tilde{x}_2 \tag{3.31}$$

where δ is a nonnegative constant. This translates to $\|b\| \le \delta$.

Lyapunov stability analysis is used to show the stability of the feedback linearization controller with the estimated state $\hat{x}_2$. If the zero state equilibrium of the nominal system tracking error dynamics is exponentially stable, then there exist a Lyapunov function $V_{con}(e)$ and strictly positive constants $\alpha_{i,}\ i = 1,...,4$ that satisfies

$$\alpha_1 \|e\|^2 \le V_{con}(e) \le \alpha_2 \|e\|^2 \tag{3.32}$$

$$\dot{V}_{con}(e) \le -\alpha_3 \|e\|^2 \tag{3.33}$$

$$\left\| \frac{\partial V_{con}(e)}{\partial e} \right\| \leq \alpha_4 \|e\| \tag{3.34}$$

The derivative of $V_{con}(e)$ along the trajectories of the perturbed system, (3.30) is given by

$$\dot{V}_{con}(e) = \dot{V}_{con}^{nom}(e) + \frac{\partial V_{con}(e)}{\partial e} b\tilde{x}_2 \tag{3.35}$$

where $\dot{V}_{con}^{nom}(e)$ is given by (3.33).

Substituting (3.33) into (3.35) and simplifying gives

$$\dot{V}_{con}(e) \leq -\alpha_3 \|e\|^2 + \delta \left\| \frac{\partial V_{con}(e)}{\partial e} \right\| \|\tilde{x}_2\| \tag{3.36}$$

Further simplification results in,

$$\dot{V}_{con}(e) \leq -\alpha_3 \|e\|^2 + \delta \alpha_4 \|\tilde{x}_2\| \|e\| \tag{3.37}$$

Now consider the composite Lyapunov function

$$V(\tilde{x}_2, e) = V_{con}(e) + V_{obs}(x) \tag{3.38}$$

for the total system (observer and controller). Then

$$\dot{V}(\tilde{x}_2, e) \leq -\alpha_3 \|e\|^2 + \delta \alpha_4 \|\tilde{x}_2\| \|e\| - \beta \|\tilde{x}_2\|^2 \tag{3.39}$$

where β is given by (3.29). Manipulation of (3.39) results in

$$\dot{V}(\tilde{x}_2, e) \leq -\begin{bmatrix} \|e\| & \|\tilde{x}_2\| \end{bmatrix} M \begin{bmatrix} \|e\| \\ \|\tilde{x}_2\| \end{bmatrix} \tag{3.40}$$

where

$$M = \begin{bmatrix} \alpha_3 & -0.5\alpha_4\delta \\ -0.5\alpha_4\delta & \beta \end{bmatrix} \tag{3.41}$$

For $\dot{V}(\tilde{x}_2, e)$ to be negative, it is sufficient that the leading principal minors of the $2x2$ matrix M be positive [22], that is

$$\alpha_3 > 0 \tag{3.42}$$

$$\delta^2 < \frac{4\alpha_3\beta}{\alpha_4^2} \tag{3.43}$$

Condition (3.42) is already satisfied. If δ satisfies (3.43), we see that $\dot{V}(\tilde{x}_2, e) < 0, \forall \tilde{x}_2 \neq 0, e \neq 0$ and the equilibrium point $(\tilde{x}_2, e) = (0,0)$ is uniform globally exponentially stable.

3.6 Simulation Results

The performance of the proposed control scheme is simulated on the MEMS electrostatic microactuator using MATLAB/SIMULINK. The reference signal used in the simulation selected such that y_r is the desired final equilibrium position and thus $\dot{y}_r = \ddot{y}_r = y_r^{(3)} = 0$.

For purposes of comparison and demonstration of the effectiveness of the controller, the open-loop system is first simulated under constant voltage actuation conditions. In Figure 3.3, the open – loop system is simulated with an applied voltage of $V_s = V_{PI}$.

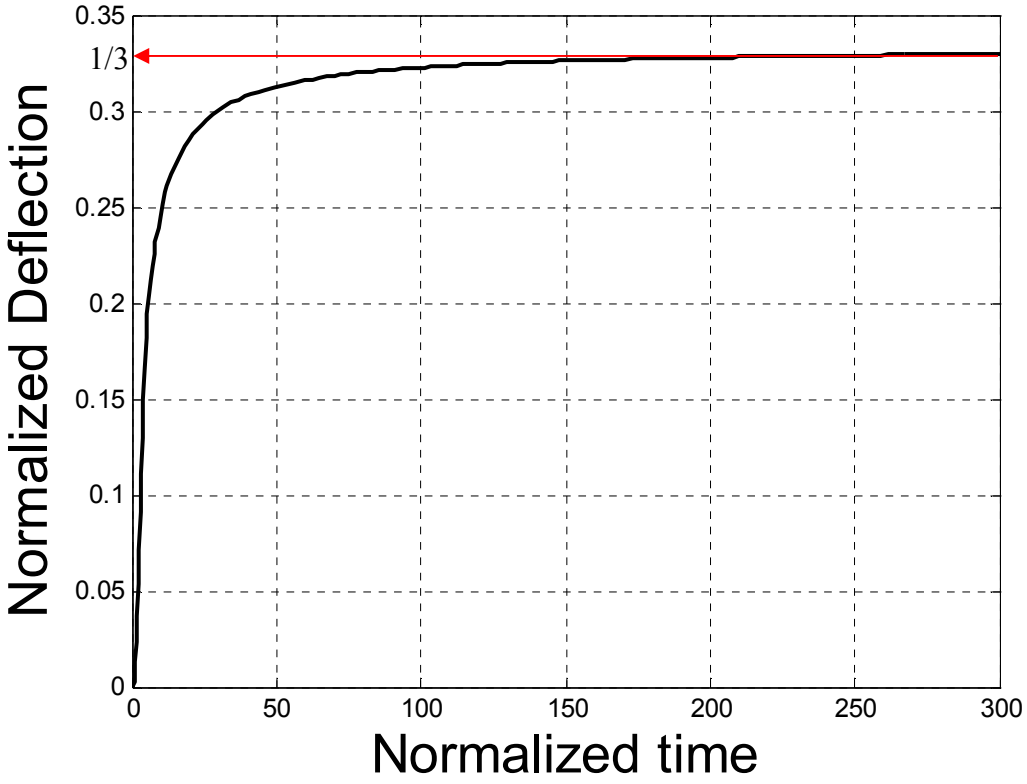

Figure 3.3 Open-loop System under Constant Voltage Actuation with $V_s = V_{PI}$

Figure 4 shows results of simulations for the open-loop system under constant voltage actuation with an applied voltage of $V_s = 1.1V_{PI}$.

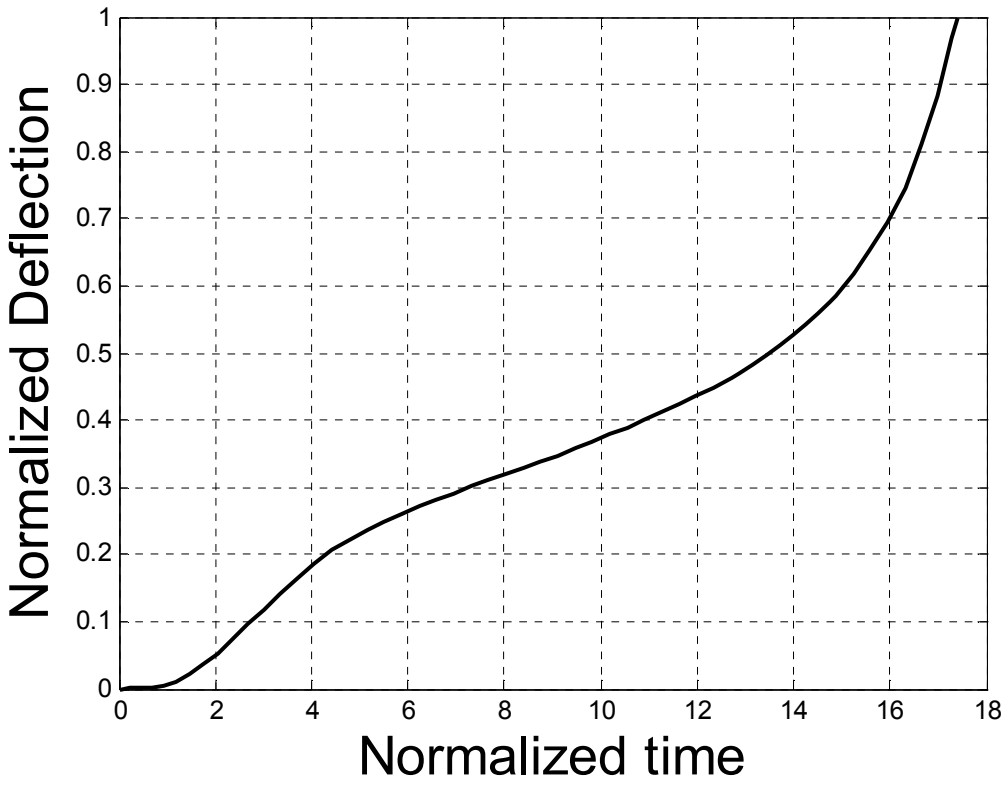

Figure 3.4 Open-loop System under Constant Voltage Actuation with $V_s = 1.1V_{PI}$

The responses in figures 3.3 and 4.4 show that with an applied voltage equal to the pull-in voltage, the system has 1 equilibrium position at a deflection of $1/3$ the nominal gap and the system has a very slow response time. Also, for an applied voltage greater than the pull-in voltage, the system has no stable equilibrium position and the electrostatic force acting on the movable plate is much greater than the restoring force resulting in its collapse to the stationary plate position.

Figure 3.5 shows results of MATLAB/SIMULINK simulations using the proposed control method for responses corresponding to a deflection of 30%, 60% and

90% of the nominal capacitive gap for a system with a damping ratio $\alpha = 1$. It is assumed that initially the movable plate is at the equilibrium position $(0 \quad 0 \quad 0)$ ie. the rest position of the microactuator. To initiate motion from the rest position, a relatively small voltage is momentarily applied to the system. A saturation block is employed to impose upper and lower bounds on the control input signal. Note that all units are non-dimensional corresponding to the normalized state space representation (3.12).

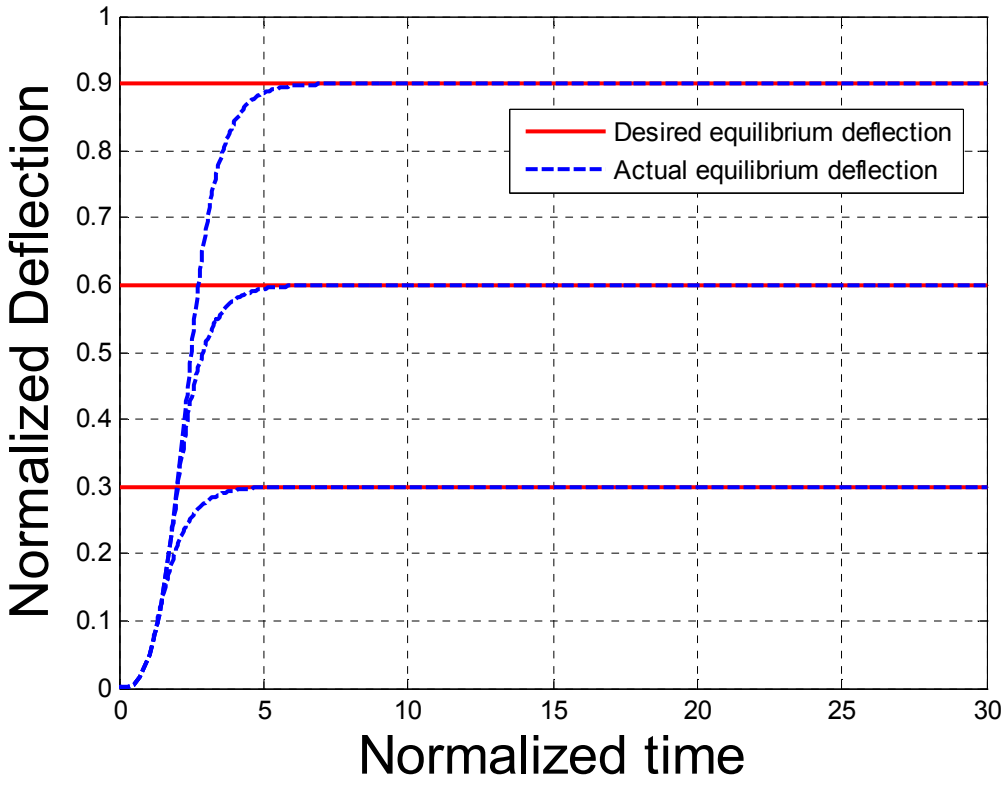

Figure 3.5 Normalized Plate Deflection vs. Normalized Time for a microactuator with a damping ratio $\alpha = 1$

Figure 3.6 show the results of simulations corresponding to a deflection of 30%, 60% and 90% of the normalized gap for three systems with damping ratios 0.1, 0.5 and 2.5.

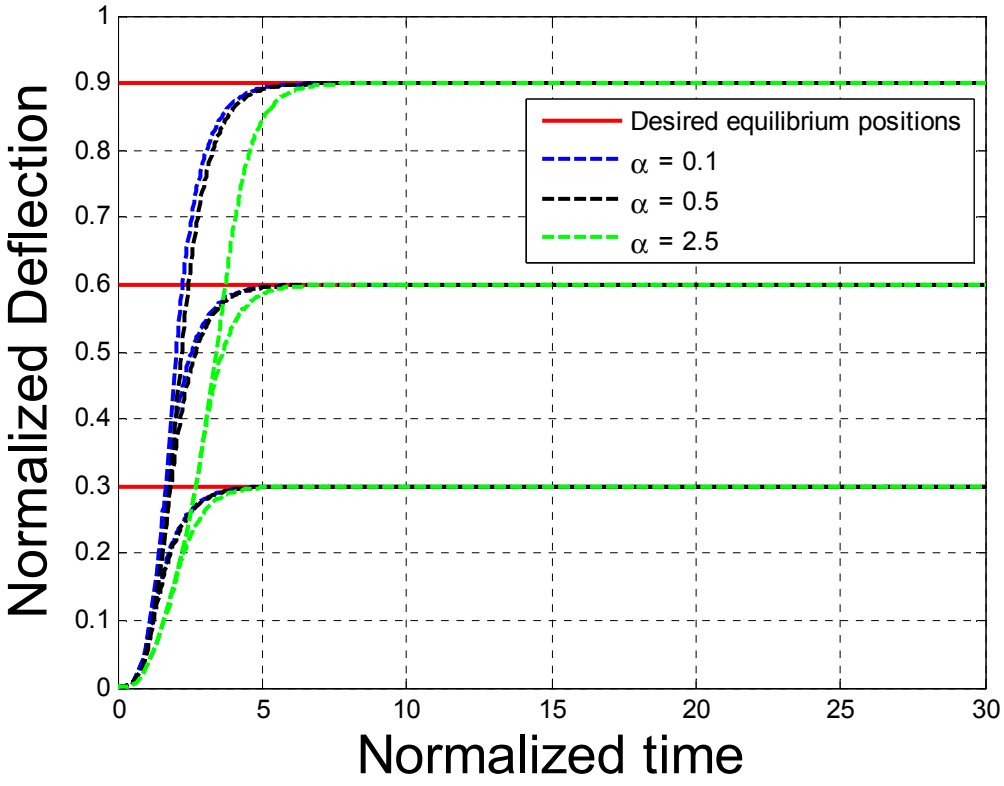

Figure 3.6 Normalized Plate Deflection vs. Normalized Time for electrostatic microactuators with damping ratio variations

The time responses in figures 3.5 and 3.6 show a fast response time with almost negligible overshoot and no oscillations. This clearly demonstrates an immense improvement in the dynamic performance of the microactuator system beyond the "pull-in" instability point. Also, the effect of damping on the system dynamic response is relatively out of merit but more pronounced for larger deflections. All simulations

were performed with the same controller designed using a nominal plant model with a damping ratio $\alpha = 1$. It can thus be inferred from the simulation results that the proposed nonlinear controller and observer design approaches presented have extremely good parameter robustness. Another interesting observation is that the initial control signal spikes due to the initial small value of charge on the movable plate makes the plates of the electrostatic microactuator initially attract each other strongly, speeding up the system response.

Because feedback and state estimation based on the measurement of the output of a system are inherently noisy, we simulate the proposed control scheme in the presence of measurement noise to investigate its noise rejection capabilities. The measurement noise is modeled as discrete-time white Gaussian distributed noise. Figure 3.7 shows the system response corresponding to 30%, 60% and 90% of the nominal capacitive gap for a system having a damping ratio of 1 under output measurement noise conditions.

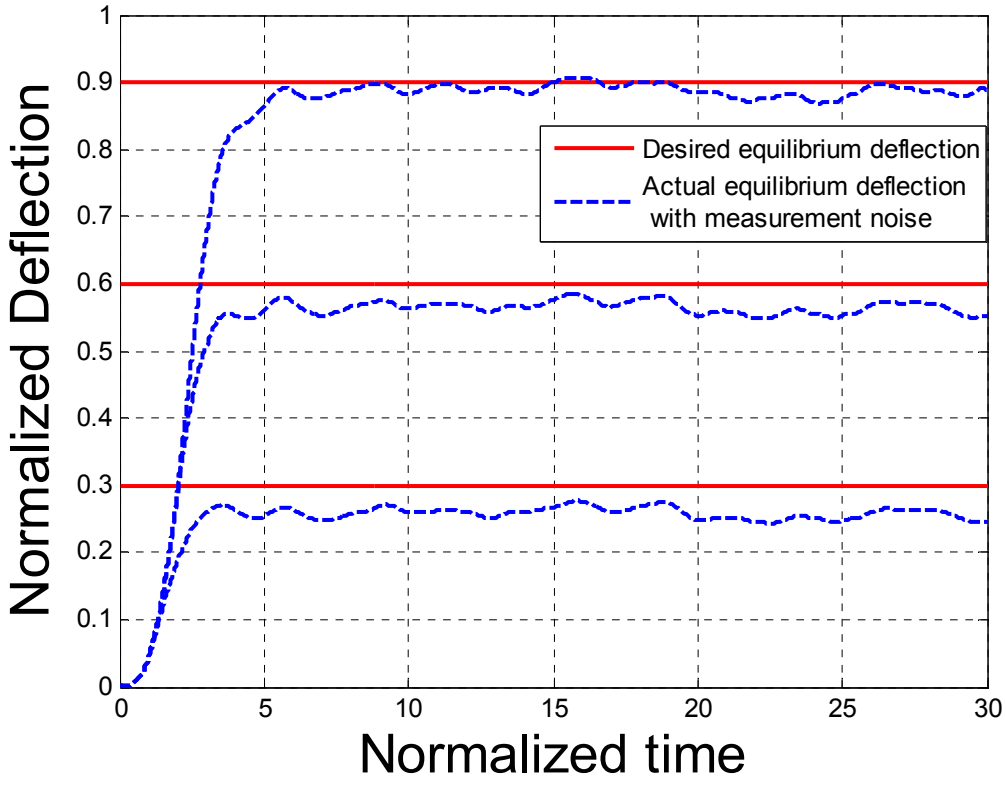

Figure 3.7 Normalized Plate Deflection vs. Normalized Time for a microactuator under output measurement noise conditions.

It is observed that in the presence of output measurement noise, the system performance deteriorates. The performance depreciation is most significant for small displacements. The relatively poor system dynamic performance may be attributed to the fact that, the measurement noise is multiplied by the observer gain in the observer. This implies that the observer gain should be carefully tuned to prevent the effect of noise from "blowing up" while not compromising on the overall system performance.

3.7 Conclusions

This paper primarily focused on the development of a nonlinear tracking control system that stabilizes electrostatic microactuators and increased the range of stable and controllable motion to the entire capacitive gap under suitable operation conditions.

An input-output feedback linearization approach to nonlinear state feedback controller design is illustrated and implemented with the aid of a nonlinear reduced-order velocity observer. The numerical simulations demonstrate explicitly that the proposed control scheme has extremely good tracking performance even in the presence of output measurement noise inherent in feedback control. The effect of the natural damping of the mechanical system on the microactuator dynamics is also appreciably diminished with this control strategy.

CHAPTER 4

A NEW DESIGN FOR FIBER-OPTIC PRESSURE MICROSENSORS

4.1 Introduction

The inherent, natural Micro electro mechanical systems (MEMS) properties of small size and potentially low cost is encouraging the liberal usage of MEMS devices in many applications hitherto dominated by macro devices. One such application which has seen tremendous increase in interest in both industry and academia is the development of fiber-optic MEMS pressure sensors.

Fiber-optic pressure microsensors offer unique benefits over electrical sensors which usually employ capacitive or piezoelectric detection schemes [23]. They are more suitable for harsh environmental applications characterized by high temperatures, high levels of electromagnetic interference, chemical attack, or in the presence of explosive materials. They feature excellent repeatability, high accuracy and reliability under varying environmental conditions. In addition operation conditions are highly consistent from one sensor to the other and they feature high resolution and sensitivity. These advantages make them suitable for delicate in-vivo and in vitro applications to aid in medical diagnosis and prognosis [24]. Fiber optic pressure sensors are mostly classified into two main categories: interferometers in which optical phase is affected and intensity-based devices in which optical intensity is modulated.

Fiber-optic microsensors contain sensing elements that mostly consists of a thin diaphragm. In the interferometers, the optical fiber is positioned close to the fiber to create a Fabry-Perot cavity. Optical interference detected with the aid of the optical fiber and optical detector is used to determine the deflection of the diaphragm, which is proportional to the applied fluid pressure. Microsensors based on Fabry-Perot interferometry fabricated directly on the tip of the optical fiber have been developed in various research studies [23] - [25]. These interferometric sensors have the advantages of ultra high resolution, accuracy and configuration versatility [32]. However, they have the disadvantages of relative measurement, fringe direction ambiguity, and costly signal processing [33]. To eliminate fringe direction ambiguity and relative measurement limitations associated with interferometric sensors, the interferometric sensors are normally designed such that it is operated over the linear range between a valley and a peak of one interference fringe. This limits the pressure sensing range.

In contrast to fiber interferometers, the intensity-based devices have the advantages of simple signal demodulation, absolute measurement, and high frequency response. Its main limitations are that, in addition to the measurand, the sensor output is also sensitive to source power variations and fiber bending losses, which are often misinterpreted as measurand changes. Real-time self-calibration to compensate for these unwanted changes is thus imperative.

In this work, a novel miniature fiber-optic pressure sensor which utilizes both optical interference and optical intensity modulation is presented. Our primary objective is to eliminate fringe direction ambiguity and relative measurement limitations

associated with interferometric sensors by the incorporation of optical intensity modulation. In the design, the fiber axis is misaligned with respect to the center of the deflecting diaphragm. In this misaligned position, when the diaphragm deflects, the light coupling from diaphragm to fiber occurs on the slope of the deformed diaphragm reducing coupling efficiency significantly. This modulated intensity is used in combination with the optical interference pattern to determine the applied pressure. Experimental results demonstrate the advantages of this improved design.

4.2 Sensor System Design and Principle of Operation

The structure of the complete fiber-optic pressure sensor system is shown in figure 4.1. It consists of the sensor, a 50/125μm graded index multimode fiber with a numerical aperture of 0.2, a 633nm HeNe laser source, and an optical detector. The multimode fiber has 2 x 2 coupler with a 50/50 split ratio.

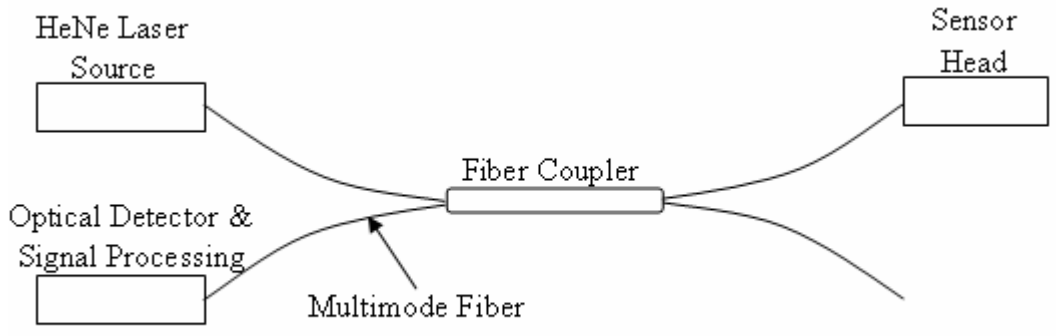

Figure 4.1 Complete Sensor System

The light from the HeNe laser source is launched into the one end of the optical fiber through a 20X objective microscope attached to a 3-DOF (degree of freedom) micro translation stage for alignment. The laser light passes through the optical fiber coupler to the sensor. The light reflected from the sensor passes through the optical fiber coupler to the optical detector which is used to get the interference pattern with the aid of a data acquisition card. With the 2 x 2 coupler with a 50/50 split ratio used, choosing any of the four legs as the input, the output is split equally between the opposite two legs. In this application, the fourth leg is unused. The reflected light which is used for pressure monitoring is split 50/50 between the two fibers on the left side of the coupler in figure 4.1. 50% of the return signal would be sent to the optical detector and 50% returned on the original input fiber connected to the source.

The sensor is formed at the tip of the optical fiber. The design of the sensor head is as shown in figure 4.2. The sensor head has a circular diaphragm with a diameter much greater than the diameter of the optical fiber core. The complete system consists of the Si diaphragm and a micromachined glass substrate with a cavity and a hole for the fiber. The Si diaphragm and glass substrates are bonded together by anodic wafer bonding. The optical fiber is placed in a capillary tube and inserted into the hole in the glass substrate. The width of the cavity between the glass surface and the fiber end is made smaller than the fiber diameter so that it serves as a stop for positioning the fiber. The fiber core axis is misaligned by a distance d from the center of the diaphragm.

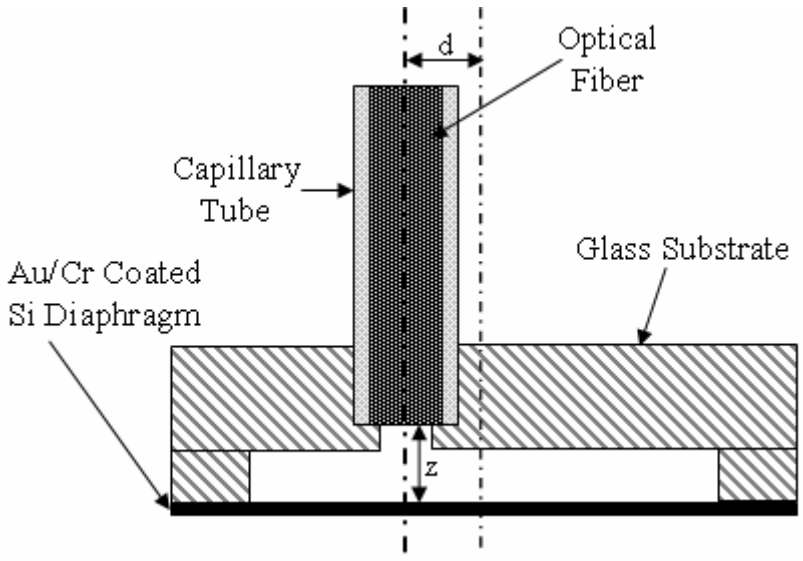

Figure 4.2 Sensor Head Design

The gap between the tip of the optical fiber and the diaphragm constitute a Fabry – Perot interferometer. The Fabry-Perot interferometer works on the principle of constructive interference. Applying pressure to the diaphragm causes a deflection of the diaphragm and modulates the air gap length. The incident light from the HeNe laser source is first partially reflected at the output fiber end glass-air interface. The remainder of the light is then modulated at the Fabry-Perot interferometer of the sensor. The light reflected by the sensor travels back along the same fiber with the light reflected from the glass-air interface to the optical detector. The interferometric superposition of the multiple reflections generates the output signal which is a function of the Fabry-Perot cavity length. A schematic of a Fabry-Perot cavity between an optical fiber and a reflective mirror is shown in figure 4.3.

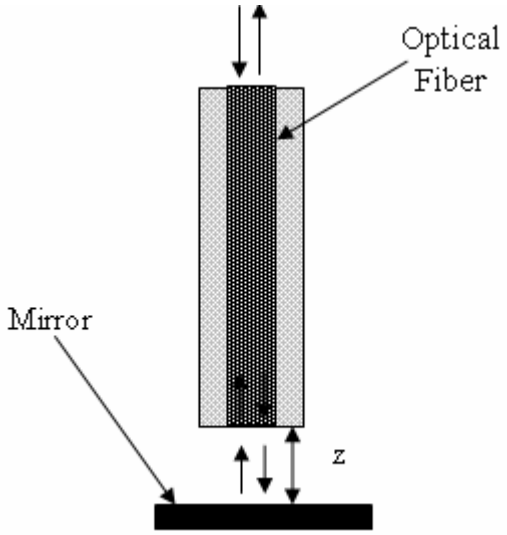

Figure 4.3 Illustration of a Fabry Perot Cavity

For an interferometric-intensity based pressure sensor, the intensity of the sensor output will change sinusoidally with the air-gap changes. In order to eliminate fringe direction ambiguity, the sensor can be designed such that it is operated within a linear range of one fringe as shown in figure 4.4. This decreases the sensing range.

In this work, we try to eliminate this limitation by designing the sensor with the fiber misaligned with respect to the center of the diaphragm. The consequence of misaligning the fiber axis with the center of the diaphragm is the introduction of more losses in the light coupling from diaphragm to fiber. This occurs because the light from the laser is reflected along the slope of the deformed diaphragm. The tradeoff is a more tedious fabrication process as a misalignment to a micron scale precision is not easy to achieve.

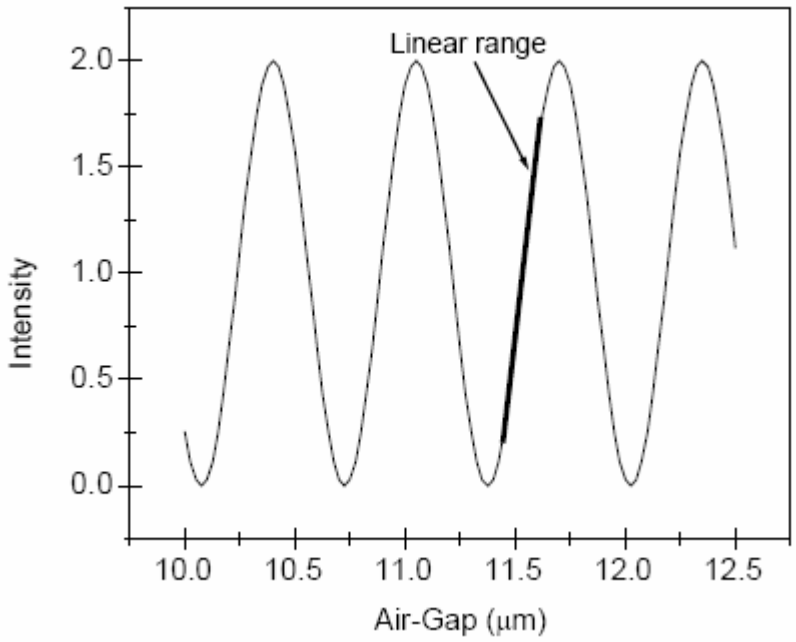

Figure 4.4 Interference Fringes versus Sensor Air-Gap

4.3 Diaphragm Deflection Analysis

The out-of-plane deflection w of a clamped circular diaphragm under a uniform applied pressure P is a function of the pressure difference and the radial distance and is given by [26], [31].

$$w(r) = \frac{Pa^4}{64D}\left[1 - \left(\frac{r}{a}\right)^2\right]^2 \qquad (4.1)$$

where r and a are the radial coordinate and diaphragm radius respectively. D is the flexural rigidity, which is a measurement of stiffness and is given by

$$D = \frac{Eh^3}{12\left(1 - v^2\right)} \qquad (4.2)$$

where $E, h, and\ v$ are Young's modulus, diaphragm thickness and Poisson's ratio respectively.

For a clamped circular diaphragm, the deflection varies from zero at the edges to the maximum value at its center. The deflection curve under pressure is obtained from (4.1) by putting it in the form

$$w(r) = w_{\max}\left[1-\left(\frac{r}{a}\right)^2\right]^2 \qquad (4.3)$$

where $w_{\max}$ is the maximum deflection which occurs at the centre of the diaphragm. Equations (4.1) and (4.3) are valid only when the deflection is less than 30% of the thickness of the diaphragm [31], which implies $y_{\max} < 0.3h$.

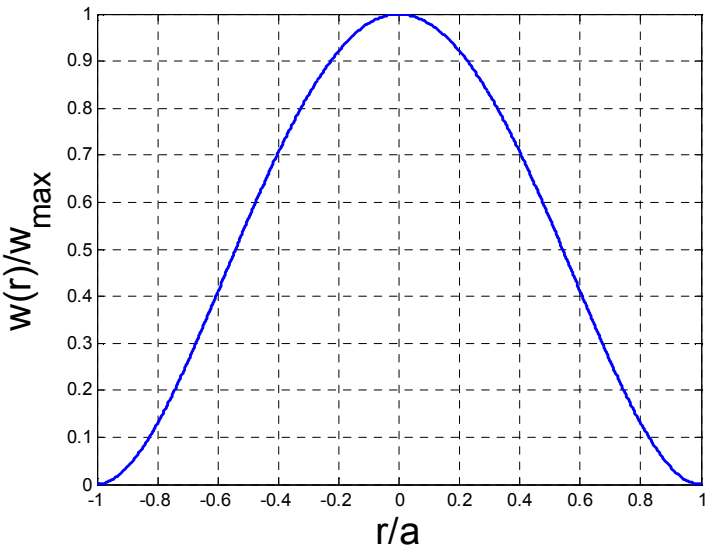

Figure 4.5 Deflection Curve of the Diaphragm under Pressure

The slope of the deformed diaphragm is given by

$$\frac{\partial w(r)}{dr} = \frac{P}{16D}\left(-a^2 r + r^3\right) \qquad (4.4)$$

The slope is maximum when $r = a/\sqrt{3}$. This implies that maximum coupling loss of the reflected light from the diaphragm due to misalignment would be obtained when the fiber is positioned at a distance of $a/\sqrt{3}$ from the center of the diaphragm. A plot of the slope of the deformed diaphragm is shown in figure 6.

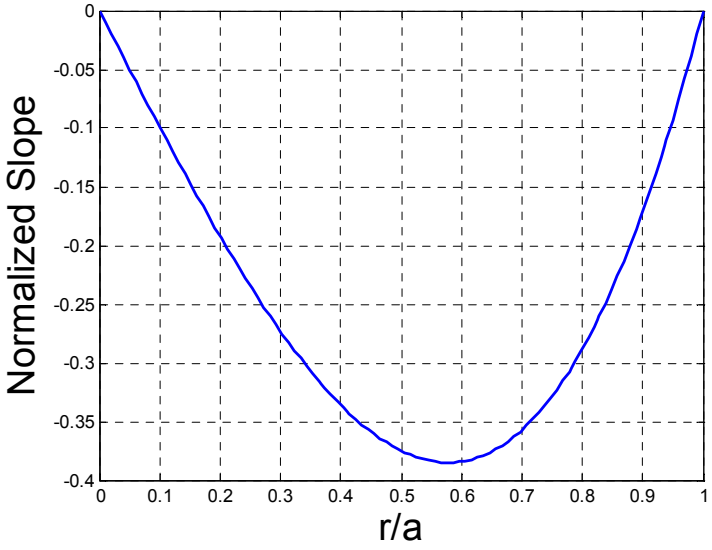

Figure 4.6 Slope of Deformed Diaphragm

4.4 Optical Analysis

The novel pressure microsensor design utilizes the increased optical intensity modulation due to the reflection from the slope of the deformed diaphragm. The main losses in the fiber coupling can be categorized into intrinsic and extrinsic losses. Due to the fact that only one optical fiber is used, Fresnel reflection loss at the fiber glass-air interface in the sensor is the only intrinsic loss in the system. The difference in the

refractive indices of the fiber glass and air reduces the optical power getting out of the optical fiber by the factor [27]

$$R = \left(\frac{n_1 - n}{n_1 + n} \right)^2 \qquad (4.5)$$

where R is the Fresnel reflection or the reflectivity at the fiber core end face, n_1 is the refractive index of he fiber core and n is the refractive index of air. Fresnel reflection is calculated to be about 4% of the incident optical power which results in a loss of 0.14dB.

To estimate the extrinsic losses in the system, the light coupling between the fiber and diaphragm is modeled as fiber to fiber coupling with an air gap of twice the length of the sensor cavity as in figure 4.7.

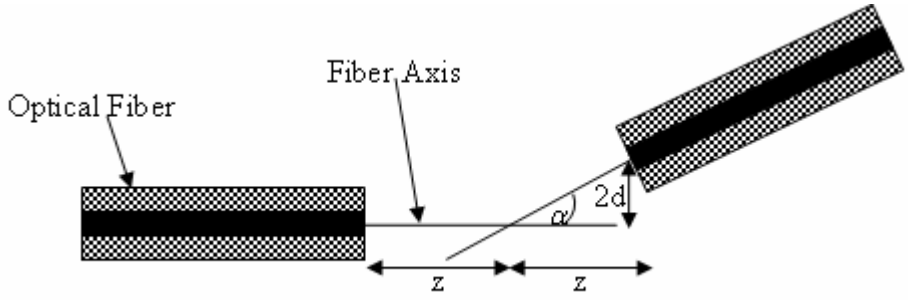

Figure 4.7 Fiber Coupling Model showing Extrinsic Mismatches

The extrinsic losses occurring in the system is a combination of losses due to radial offset, air gap separation and angular misalignment. It should be noted that the losses due to radial offset and angular misalignment are a consequence of the misalignment between the fiber axis and the center of the diaphragm.

From the sensor head design in figure 4.2 and the coupling model in figure 4.7, applying a pressure P causes a deflection w of the diaphragm reducing the air gap length to $z-w$ and causing a fiber coupling tilt angle of α with a corresponding axial displacement of $(z-w)\alpha$. There is no general equation describing the combinations of extrinsic mismatches. Therefore, the behavior of losses in the presence of single coupling errors is discussed.

Longitudinal (end) separation occurs when the fibers have the same axis, but have a gap $2z$ between their end faces. [28], [29]. Using a geometrical optics approach, the coupling efficiency of two identical graded index fibers with a gap is [29]

With

$$\eta = \frac{1}{N^2}\frac{g+2}{g} - \frac{4}{\pi N^2}\frac{g+2}{g}\int_0^1 \rho d\rho \int_0^{\frac{\pi}{2}} \frac{1}{1+W_g^2} d\phi \tag{4.6}$$

$$W_g = \min\left[\frac{2\rho}{\zeta}\cos\phi, \sqrt{\frac{N^2\left(1-\rho^g\right)}{1-N^2\left(1-\rho^g\right)}}\right] \tag{4.7}$$

$$\rho = (r/a) \tag{4.8}$$

where g is the profile exponent ($g=2$ for parabolic index profile), $\zeta = \left(2z/a\right)$ is the normalized air gap distance, a is the core radius, N is the on-axis numerical aperture of the fiber and r is the distance from the fiber axis.

Angular misalignment results when the two fiber axes form an angle so that the fiber end surfaces are no longer parallel. Using geometrical optics, the coupling efficiency of two identical graded index fibers with a parabolic index profile is found to be [28]

$$\eta = \frac{4}{\pi}\left[\frac{1}{2}\arccos\left(\frac{\gamma}{\sqrt{2\Delta}}\right) - \frac{\gamma}{\sqrt{2\Delta}}\sqrt{1-\frac{\gamma^2}{2\Delta}}\left(\frac{5}{6}-\frac{1}{3}\frac{\gamma^2}{2\Delta}\right)\right] \tag{4.9}$$

where Δ is the relative refractive index difference and $\gamma = \sin(\alpha/2)$ with α being the fiber tilt angle.

Radial offset (axial or lateral displacement) results when the axes of the two fibers are parallel but separated by a distance $2d$ radially. The fiber coupling efficiency of two identical graded index fibers with parabolic index profile is [28]

$$\eta = \frac{4}{\pi}\left\{\frac{1}{2}\arccos\left(\frac{d}{a}\right) - \frac{d}{a}\sqrt{1-\left(\frac{d}{a}\right)^2}\left[\frac{5}{6}-\frac{1}{3}\left(\frac{d}{a}\right)^2\right]\right\} \tag{4.9}$$

Plots of the coupling efficiencies and corresponding attenuations in dB are shown in [28, 29, 30]. From the plots it can be inferred that radial offset and angular misalignment have equal effect on the coupling loss, and they lead to greater losses than end separation. Thus, with the introduction of radial offset and angular misalignment losses in the microsensor system, the optical intensity modulation with changes in applied pressure and hence the sensitivity would increase appreciably.

4.5 Experimental Setup

An experimental set up which mimics the behavior of the actual pressure microsensor was used to investigate the performance characteristics of the microsensor. The setup is similar to figure 4.1 except that the sensor head was not fabricated at the tip of the optical fiber. In the experiment, the end of the optical fiber (connected to the sensor head in figure 4.1) was attached to a 2-DOF precision stage motorized and set against a fine Au/Cr plated fixed silicon piece. The precision motorized stage comprises

a motorized actuator and a motorized rotator for varying the air gap length between the fiber and mirror and the fiber tilt angle respectively. The laser light generated by the HeNe source is modulated in the sensor cavity and reflected back along the same fiber to an optical detector. The reflected signal data obtained from the detector is captured with a data acquisition card for analysis.

The central idea behind this experimental procedure is that when pressure acts on the actual diaphragm, the corresponding deflection of the diaphragm changes the air gap length and the reflection occurring on the slope of the deformed diaphragm means a change in angular misalignment of the reflected light with respect to the fiber axis. This is equivalent to having a fixed diaphragm and changing the fiber position and tilt angle with respect to the diaphragm. The pressure – deflection characteristics of (4.1) and (4.3) is comparable to the distance and tilt angle variation of the optical fiber in this experiment.

4.6 Experimental Results

The diaphragm deflection relation of equation (4.1) was simulated with the fiber at different radial locations to show the effect of the extrinsic mismatches on the coupling efficiency. The system parameters used in the simulations are:

Initial cavity length $z = 30\mu m$.

Relative refractive index difference $\Delta = 0.01$

Numerical Aperture $N = 0.2$

Profile exponent $g = 2$ (parabolic index profile)

Fiber Core radius $b = 25 \times 10^{-6} m$

Young's modulus of silicon E = 160 x 10^{9}Nm^{-2}

Poisson's ratio v = 0.22

Diaphragm thickness h = 4 x 10^{-6}m

Diaphragm radius a = 300 x 10^{-6}m

Wavelength of laser source λ = 633nm.

Figure 4.8 shows the effect of changes in the air gap separation due to applied pressure on the coupling efficiency simulated at different radial locations.

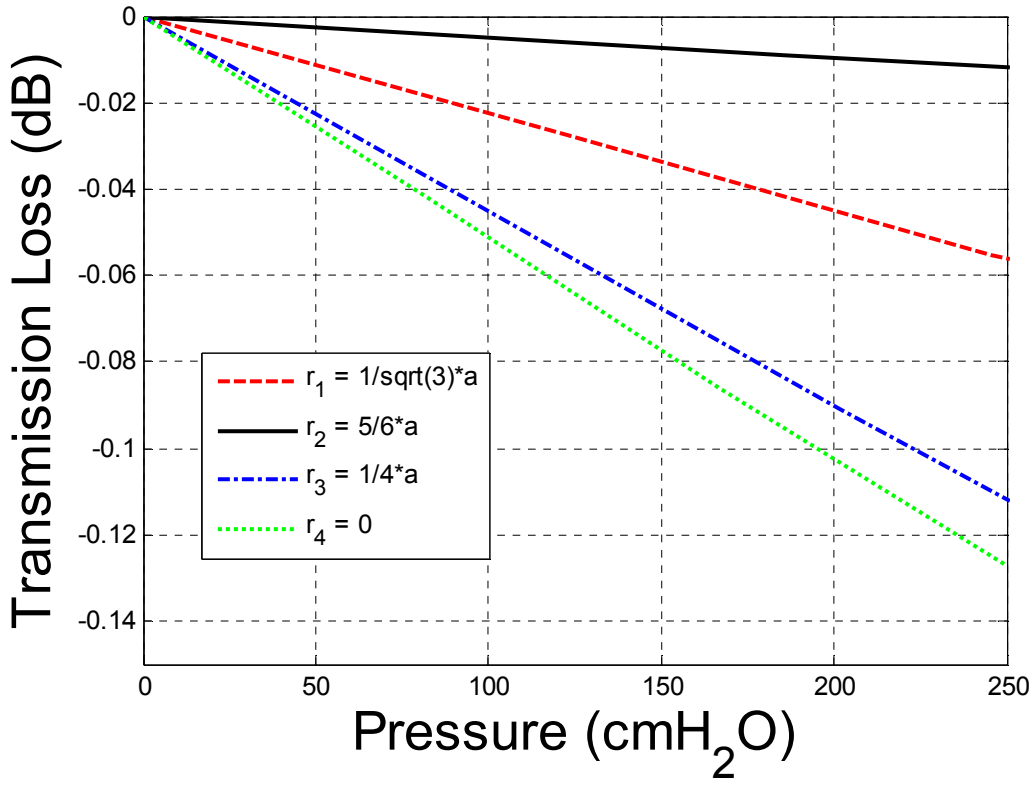

Figure 4.8 Simulated Coupling Efficiency due to End Separation at Different Radial Locations

Figure 4.9 shows the effect of angular misalignment on the coupling efficiency due to applied pressure simulated at different radial locations.

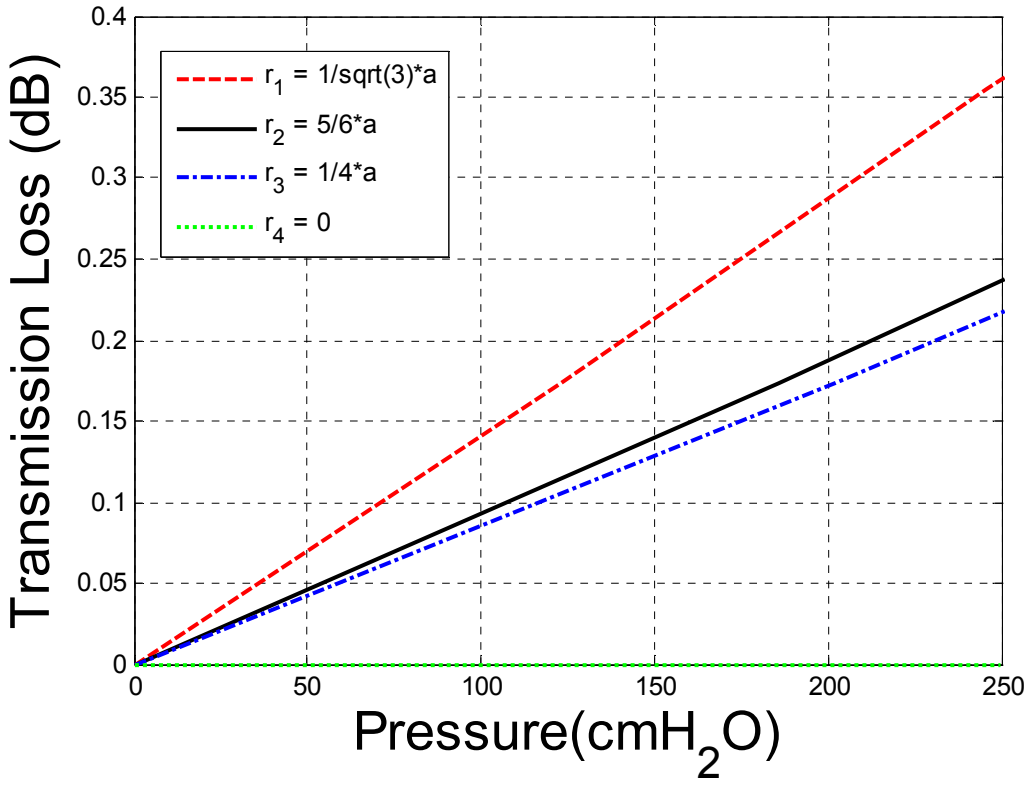

Figure 4.9 Simulated Coupling Efficiency due to Angular Misalignment at Different Radial Locations

The effect of radial offset is comparable to that of angular misalignment. From figures 4.8 and 4.9, it is seen that when pressure increases, the air gap separation reduces and there is a gain in optical intensity, whilst angular misalignment increases resulting in a decrease in intensity. Also, the effects of angular misalignment and radial offset are more pronounced than gap separation. This results in a net coupling efficiency loss with applied pressure. Note that the effect of angular misalignment is maximum at $r = a/\sqrt{3}$

which agrees with the diaphragm deflection analysis presented in section 4.3. The transmitted power of the reflected signal from the mirror was measured for a 10 μm change in air gap at preset fiber tilt angles. The tilt angles were preset because it was not possible to accurately estimate the air gap length when the fiber tilt angle and the air gap length were changed simultaneously. This is to mimic the behavior of the actual sensor which has both the gap and fiber tilt angles changing with applied pressure. The measured power in volts after signal processing is shown in figure 4.10.

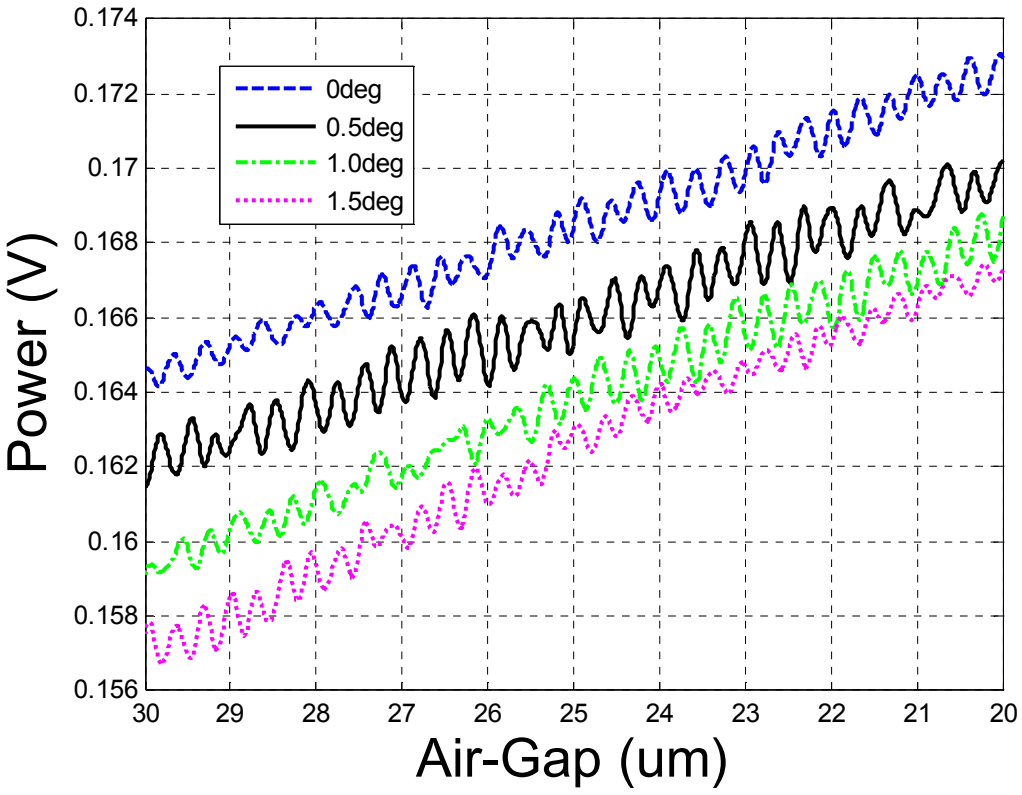

Figure 4.10 Power Variations at Various Tilt Angles and Cavity Lengths

It is observed that the periodic length of the oscillating phenomenon is roughly half the optical wavelength, which is 316.5 nm and it agrees with that of a Fabry-Perot Cavity. Also the intensity decreases as the tilt angle increases. Figure 4.11 shows the combination of experimental results of transmission loss (power change) with respect to simulated pressure-diaphragm characteristics.

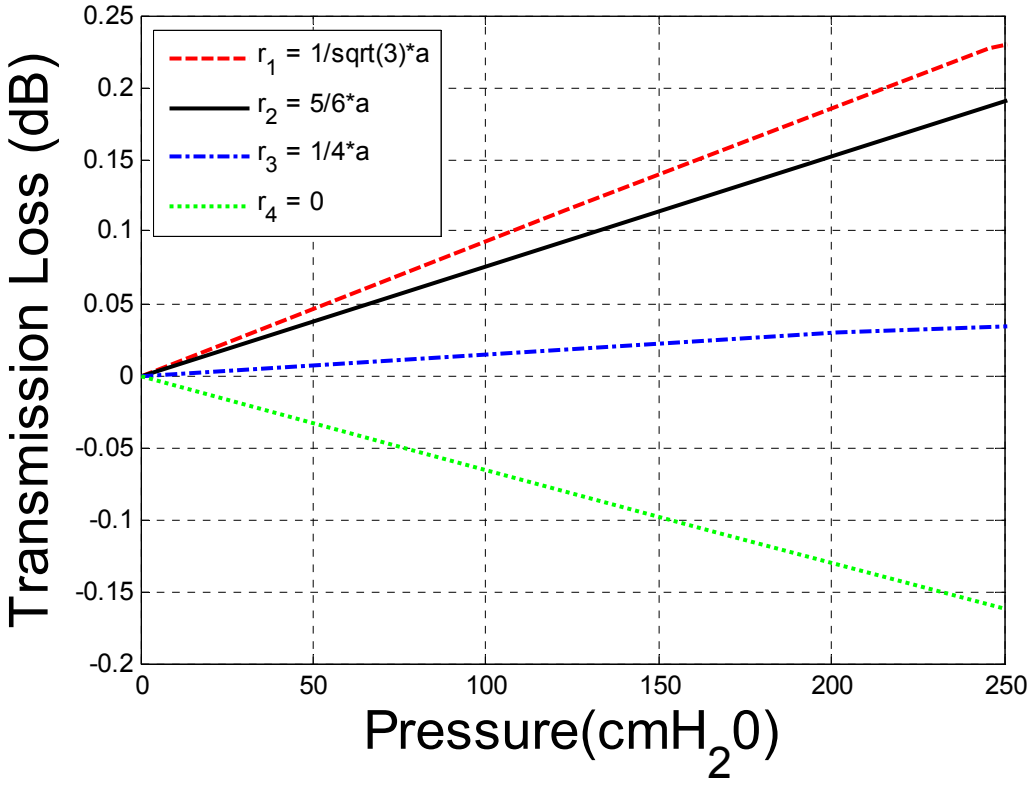

Figure 4.11 Experimentally obtained Transmission Loss with respect to Simulated Pressure Changes

According to figure 4.11, the sensor with the fiber located at a radial distance of $r = a/\sqrt{3}$ has the highest sensitivity with respect to applied pressure. Compared to the fiber located at the centre of the diaphragm, the increase in sensitivity is about 66%.

4.7 Conclusions

A new design for a fiber optic pressure sensor was designed, analyzed and experimentally tested. This design has the potential to reduce the limitations of fringe direction ambiguity in interferometric-intensity based pressure sensors. The sensitivity of this design is about 66% higher than conventional interferometric-intensity based pressure sensors. This sensor can be fabricated with simple micromachining processes compatible with MEMS.

REFERENCES

[1] R. T. Chen, H. Nguyen and M. C. Wu, "A high-speed low-voltage stress-induced micromachined 2x2 optical switch," IEEE Photonics Technology Letters, Vol. 11, No. 11, 1999.

[2] C. R. Giles, V. Aksyuk, B. Barber, R. Ruel, L. Stulz, and D. Bishop, "A silicon MEMS optical switch attenuator and its use in light wave subsystems," IEEE Journal of selected topics in Quantum Electronics, Vol. 5, No. 1, pp. 18-25, 1999.

[3] J-J. Slotine and W. Li, Applied Nonlinear Control, Prentice Hall, New Jersey.

[4] D. H. S. Maithripala, J. M. Berg, and W. P. Dayawansa, "Nonlinear dynamic output feedback stabilization of electrostatically-actuated MEMS," Proc. of the CDC, Maui, HW, 2003.

[5] R. Rajamani, "Observers for lipschitz nonlinear systems," IEEE Transactions on Automatic Control, Vol. 43, No. 3, March 1998.

[6] F. E. Thau, "Observing the state of nonlinear dynamic systems," Int. J. Contr., Vol. 17, No. 3, 1973.

[7] R. V. Patel and M. Toda, "Quantitative measures of robustness in multivariable systems," in Proc. American Control Conf., San Francisco, CA, 1980, p. TP8-A.

[8] A. Isidori, Nonlinear Control Systems, Third Edition, Springer, 1995.

[9] J. Li, Q. X. Zhang, A. Q. Liu, "Advanced fiber optical switches using deep RIE (DRIE) fabrication," Sensors and Actuators A: Physical , Vol. 102, No. 3, pp 286-295, 2003.

[10] A. Q. Liu, X. M. Zhang, C. Lu, F. Wang, C. Lu and Z. S. Liu, "Optical and mechanical models for a variable optical attenuator using a micromirror drawbridge," J. Micromech. Microeng., Vol. 13, pp 400-411, 2003.

[11] S. D. Senturia, Microsystem Design, Kluwer Academic Publishers, November 2000.

[12] B. Borovic, C. Hong, A. Q. Liu, L. Xie and F. L. Lewis, "Control of a MEMS optical switch," Proc. of the CDC, Bahamas, 2004.

[13] J. I. Seeger and S. B. Crary, "Stabilization of Electrostatically Actuated Mechanical Devices," International Conference on Solid-State Sensors and Actuators (Transducers '97), Chicago, pp. 1133-1136, June 16-19, 1997.

[14] S. D. Senturia, Microsystem Design, Kluwer Academic Publishers, November 2000.

[15] J. Pons-Nin, A. Rodriguez and L. M. Castaner, "Voltage and Pull-In Time in Current Drive of Electrostatic Actuators," J. Microelectromechanical Systems, Vol. 11, NO. 3, June 2002.

[16] E. S. Hung and S. D. Senturia, "Extending the travel range of analog-tuned electrostatic actuators," J. Microelectromechanical Systems, Vol. 8, NO. 4, pp. 497-505, Dec. 1999.

[17] Y. Nemirovsky and O. Bochobza-Degani, "A methodology and model for the pull-in parameters of electrostatic actuators," J. Microelectromechanical Systems, Vol. 10, NO. 4, pp. 601-615, Dec. 2001.

[18] D. H. S. Maithripala, J. M. Berg, and W. P. Dayawansa, "Capacitive stabilization of an electrostatic actuator: An Output Feedback Viewpoint," Proc. of the American Control Conference, Denver, CO, pp. 4053-4058, June 4-6, 2003.

[19] R. Nadal-Guardia, A. Dehe, R. Aigner and L. M. Castaner, "Current Drive Methods to Extend the Range of Travel of Electrostatic Microactuators Beyond the Voltage Pull-In Point," J. Microelectromechanical Systems, Vol. 11, NO. 3, pp. 255-263, June 2002.

[20] M. Zahn, Electromagnetic Field Theory: A problem Solving Approach, John Wiley & Sons, New York, 1979.

[21] D. G. Luenberger, Introduction to Dynamic Systems - Theory, Models, & Applications, John Wiley & Sons, 1979.

[22] F.L. Lewis, Optimal Estimation: With an Introduction to Stochastic Control Theory, John Wiley and Sons, New York, April 1986.

[23] Y. Zhu, and A. Wang, "Miniature Fiber-Optic Pressure Sensor," IEEE Photonics Technology Letters, Vol. 17, No. 2, February 2005.

[24] S. Chen, C. Pislaru, R. R. Kinnick, D. A. Morrow, K. R. Kaufman and J. F. Greenleaf, "Evaluating the Dynamic Performance of a Fiber-Optic Pressure Microsensor," Institute of Physics Publishing, Physiological Measurement, 26, N13-N19, 2005.

[25] K. Totsu, Y. Haga, and M. Esashi, "Ultra – Miniature Fiber-Optic Pressure Sensor using White Light Interferometry," Journal of Micromechanics and Microengineering, 15 pp. 71-75, 2005.

[26] S. Timoshenko and S. Woinosky-Krieger, Theory of Plates and Shells, McGraw-Hill Classic Textbook Reissue, 1987.

[27] G. Keiser, Optical Fiber Communications, Third Edition, McGraw-Hill, 2000.

[28] W. van Etten and J. van der Plaats, Fundamentals of Optical Fiber Communications, Prentice Hall International (UK) Ltd., 1991.

[29] W. van Etten, W. Lambo, and P. Simons, "Loss in Multimode Fiber Connections with a Gap," Applied Optics, Vol. 24, No. 7, April 1985.

[30] D. Opielka and D. Rittich, "Transmission Loss caused by an Angular Misalignment between two Multimode Fibers with Arbitrary Profile Exponents," Applied Optics, Vol. 22, No. 7, April 1983.

[31] M. Di Giovanni, Flat and Corrugated Diaphragm Design Handbook, Marcel Dekker Inc., New York, 1989.

[32] T. G. Giallorenzi, J. A. Bucaro, A. Dandridge, G. H. Siegel, Jr., J. H. Cole, S. C. Rashleigh, and P. G. Priest, "Optical Fiber Sensor Technology," IEEE Quantum Electron., vol. QE-18, pp. 626–665, 1982.

[33] K. A. Murphy, M. F. Gunther, A. M. Vengsarkar, and R. O. Claus, "Quadrature Phase-Shifted, Extrinsic Fabry–Pérot Optical Fiber Sensors," Opt. Lett.., vol. 16, pp. 273–275, 1992.

BIOGRAPHICAL INFORMATION

Kwadwo Osei Owusu received the B.S degree in Electrical and Electronic Engineering from the Kwame Nkrumah University of Science and Technology, Ghana, in 2001. He worked in the electrical power generation and transmission industries in Ghana for 2 years. Since 2004, he has been a Master of Science student in Electrical Engineering at the University of Texas at Arlington. His current research interests include Control Systems design, prototyping and implementation, and the design, control and development of MEMS devices.